

A simple method to simulate thermo-hydro-mechanical processes in leakoff-dominated hydraulic fracturing with application to geological carbon storage

Xin Ju¹, Pengcheng Fu¹, Randolph Settegast¹, and Joseph Morris¹

¹Lawrence Livermore National Laboratory

February 01, 2021

Abstract

A potential risk of injecting CO₂ into storage reservoirs with marginal permeability ([?] 10-14 mD) is that commercial injection rates could induce fracturing of the reservoir and/or the caprock. Such fracturing is essentially fluid-driven fracturing in the leakoff-dominated regime. Recent studies suggested that fracturing, if contained within the lower portion of the caprock complex, could substantially improve the injectivity without compromising the overall seal integrity. Modeling this phenomenon entails complex coupled interactions among the fluids, the fracture, the reservoir, and the caprock. We develop a simple method to capture all these interplays in high fidelity by sequentially coupling a hydraulic fracturing module with a coupled thermal-hydrological-mechanical (THM) model for nonisothermal multiphase flow. The model was made numerically tractable by taking advantage of self-stabilizing features of leakoff-dominated fracturing. The model is validated against the PKN solution in the leakoff-dominated regime. Moreover, we employ the model to study thermo-poromechanical responses of a fluid-driven fracture in a field-scale carbon storage reservoir that is loosely based on the In Salah project's Krechba reservoir. The model reveals complex yet intriguing behaviors of the reservoir-caprock-fluid system with fracturing induced by cold CO₂ injection. We also study the effects of the in situ stress contrast between the reservoir and caprock and thermal contraction on the vertical containment of the fracture. The proposed model proves effective in simulating practical problems on length and time scales relevant to geological carbon storage.

1 **A simple method to simulate thermo-hydro-mechanical processes in leakoff-dominated**
2 **hydraulic fracturing with application to geological carbon storage**

3
4 Xin Ju, Pengcheng Fu*, Randolph Settegast, Joseph Morris

5
6 Atmospheric, Earth, and Energy Division, Lawrence Livermore National Laboratory, Livermore,
7 CA 94550 USA.

8
9 *Corresponding author: fu4@llnl.gov

10
11 Abstract: A potential risk of injecting CO₂ into storage reservoirs with marginal permeability
12 ($\lesssim 10^{-14}$ m²) is that commercial injection rates could induce fracturing of the reservoir and/or the
13 caprock. Such fracturing is essentially fluid-driven fracturing in the leakoff-dominated regime.
14 Recent studies suggested that fracturing, if contained within the lower portion of the caprock
15 complex, could substantially improve the injectivity without compromising the overall seal
16 integrity. Modeling this phenomenon entails complex coupled interactions among the fluids, the
17 fracture, the reservoir, and the caprock. We develop a simple method to capture all these
18 interplays in high fidelity by sequentially coupling a hydraulic fracturing module with a coupled
19 thermal-hydrological-mechanical (THM) model for nonisothermal multiphase flow. The model
20 was made numerically tractable by taking advantage of self-stabilizing features of leakoff-
21 dominated fracturing. The model is validated against the PKN solution in the leakoff-dominated
22 regime. Moreover, we employ the model to study thermo-poromechanical responses of a fluid-
23 driven fracture in a field-scale carbon storage reservoir that is loosely based on the In Salah

24 project's Krechba reservoir. The model reveals complex yet intriguing behaviors of the
25 reservoir-caprock-fluid system with fracturing induced by cold CO₂ injection. We also study the
26 effects of the *in situ* stress contrast between the reservoir and caprock and thermal contraction on
27 the vertical containment of the fracture. The proposed model proves effective in simulating
28 practical problems on length and time scales relevant to geological carbon storage.

29

30 Keywords: Geologic carbon storage, CO₂ fracturing, THM coupled modeling, multiphase
31 multicomponent fluid flow, supercritical CO₂

32 **1 Introduction**

33

34 Geological carbon storage (GCS) is a promising measure to mitigate the effect of anthropogenic
35 greenhouse gas emissions on climate change (Pacala and Socolow, 2004; International Energy
36 Agency, 2010). To have a meaningful impact on the net CO₂ emission through GCS requires
37 injecting a large quantity of CO₂ into subsurface geological reservoirs (Orr, 2009; Haszeldine,
38 2009). Existing pilot and experimental GCS projects mainly focus on storage reservoirs with
39 ideal conditions, such as high porosity and high permeability (typically in the range of hundreds
40 to thousands of millidarcy (1 mD = 10⁻¹⁵ m²)). Considering that high quality reservoirs do not
41 necessarily exist near CO₂ sources, the utilization of less favorable reservoirs, such as those with
42 marginal permeabilities (i.e. low tens of mD), can significantly improve the commercial viability
43 of CGS. In particular, recent commercial-scale field tests demonstrate that many such low
44 permeability reservoirs have enormous CO₂ sources nearby and also enjoy easy access to drilling
45 and comprehensive monitoring systems (Mito et al., 2008, Rinaldi et al, 2013). One good
46 example of such sites is In Salah, Algeria, where a large amount of CO₂ source from nearby

47 natural gas production was injected into several storage reservoirs with marginal permeabilities
48 (around 10 mD) (Iding and Ringrose, 2010; Rinaldi et al., 2013). Therefore, understanding CGS
49 in reservoirs with marginal permeability is of great significance.

50 The main challenge facing injection into marginal-permeability reservoirs is the low injectivity
51 under the pressure constraints that prevent fluid-driven fractures, namely, hydraulic fractures,
52 from occurring in storage reservoirs. Previous studies showed that using a low injection rate that
53 complies with the pressure constraint cannot achieve even a moderate commercial-level injection
54 rate, i.e. a million-metric ton per year (Fu et al., 2017). However, recent studies postulated that
55 the issue of low injectivity in marginal-permeability reservoirs might be effectively and safely
56 mitigated if injection-triggered hydraulic fractures can be contained within reservoir rocks or the
57 lower portion of the caprock without jeopardizing the overall seal integrity of the caprock
58 complex (White et al., 2014; Fu et al., 2017). Circumstantial field data and observations from the
59 In Salah site also suggest the possible existence of such postulated scenarios (Bohloli et al.,
60 2017; Oye et al., 2013; White et al., 2014).

61 Modeling hydraulic fracturing in marginal-permeability GCS reservoirs entails the simulation of
62 many complex processes: multiphase multicomponent fluid flow and heat transfer within
63 fractures and matrix, mass and heat exchanges between fracture and matrix flows, poro/thermo-
64 elastic deformation of solid rocks, and fracture propagation. Although many numerical studies
65 have tackled this challenging task, significant simplifications had been made to mitigate various
66 numerical challenges. These simplifications could be broadly divided into two groups: (1)
67 treating hydraulic fractures as a highly permeable porous zone and (2) simplifying multiphase
68 and nonisothermal flow behaviors of injected CO₂.

69 The first group of works typically simplify the dynamic interactions between fracture
70 propagation and matrix flows and also neglect some key characteristics of hydraulic fractures
71 (e.g. Morris et al., 2011; Pan et al., 2012; Raziperchikolaei et al., 2013; Sun et al., 2016). In
72 other words, these are not designed to accurately predict the coupled thermo-hydro-mechanical
73 (THM) responses of reservoir and caprocks once fluid-driven fractures are created. Many models
74 in this category employ a continuum-based method, such as the dual porosity models and dual
75 permeability models (e.g. Guo et al., 2017; Li and Elsworth 2019; Fan et al., 2019), neither of
76 which could represent the complex flow behaviors associated with a propagating fracture.
77 Moreover, works that attempt to capture geomechanical responses of hydraulic fractures often do
78 not address complexities caused by an evolving fracture tip (e.g. Gor et al. 2014; Eshiet and
79 Sheng 2014; Vilarrasa et al., 2014). In other words, they cannot explicitly depict the evolution of
80 fracture extents and shapes which is critical to evaluating fracture containment (Rutqvist et al.,
81 2016; Ren et al., 2017; Vilarrasa et al., 2017; Sun et al., 2017).

82 The second group of works, on the other hand, strive to capture essential features associated with
83 hydraulic fracturing, such as fracturing propagation, seepage (leakoff) of fluid through fractures
84 into reservoirs, and strong nonlinearity of the coupling between fracture permeability and
85 hydraulic aperture (Fu et al., 2017; Culp et al., 2017; Salimzadeh et al., 2017; Salimzadeh et al.,
86 2018; Gheibi et al. 2018; Mollaali et al., 2019; Yan et al., 2020), but substantially simplify fluid
87 flow characteristics unique to supercritical CO₂ flow in a saline reservoir. The works of Fu et al.
88 (2017) and Yan et al. (2020) focused on modeling isothermal fluid flow in porous media and
89 ignored the thermal responses of fractures in the storage reservoir. However, these responses
90 have a great impact on caprock integrity (Vilarrasa et al., 2014; Salimzadeh et al., 2018). The
91 simulations conducted by Salimzadeh et al. (2018) used a surrogate flow model—single-phase

92 flow model— for simulating two-phase CO₂ flow, neglecting the pressure- and temperature-
93 dependency of the PVT (pressure, volume, temperature) properties and multiphase flow of
94 supercritical CO₂. In addition to discrete fracture models used by the above studies, smeared
95 fracture models, such as the phase field method (Francfort and Marigo, 1998; Francfort et al.,
96 2008), have also been adapted to address hydraulic fracturing related to CO₂ injection. Although
97 it is straightforward to integrate the mass and energy conservations of CO₂ into the general
98 formulation of the phase field method and to consider complex fracture processes (e.g. Culp et
99 al., 2017; Mollaali et al., 2019), the smearing nature of this approach, nonetheless, poses
100 stringent requirements on mesh refinement and adaptivity to accurately reconstruct the
101 displacement discontinuities across the fracture surface (Lecampion et al., 2017). This numerical
102 challenge has limited the application of the phase field to small-scale simulations (Mollaali et al.,
103 2019). According to the latest review on the modeling of caprock integrity (Paluszny et al. 2020),
104 a fully coupled 3D model that can capture the complex interplay among CO₂ injection, reservoir
105 responses, and the propagation of hydraulic fractures at the field-scale is not currently available.
106 The scarcity of such models is likely owing to the lack of a modeling scheme that can effectively
107 and efficiently simulate the inherent complexity of hydraulic fracturing in marginal-permeability
108 GCS reservoirs.

109 The objective of this study is to develop a modeling scheme that effectively and efficiently
110 simulates hydraulic fracturing in GCS reservoirs and to study the mechanisms of fracture
111 containment within the caprock formations. The proposed scheme is particularly designed to
112 simulate the interactions between coupled THM processes in a CO₂ storage system (reservoir
113 and caprock) and the propagation of a fluid-driven fracture in the so-called “leakoff-dominated”
114 regime (Bunger et al., 2005; Garagash et al., 2011). As revealed by Fu et al. (2017), hydraulic

115 fracture propagation driven by CO₂ injection into a storage reservoir is expected to be in this
116 regime, in which the majority of the injected fluid leaks from the hydraulic fracture and is stored
117 in the storage reservoir. The propagation rate of the fracture is dominated by the leakoff rate into
118 the reservoir. Mechanical responses of the fracture do not strongly affect the propagation rate, in
119 sharp contrast to fracture behavior in the so-called storage-dominated and toughness-dominated
120 regimes. This particular feature enables us to couple hydraulic fracturing and the associated rock
121 deformation with reservoir flow in a simple yet sufficiently accurate way.

122 This paper proceeds as follows. Section 2 describes the mathematical formulations of a coupled
123 THM model and the proposed modeling scheme that couples the THM model with a fracture
124 mechanics module. The underlying rationale of this scheme is also discussed in this section.
125 Section 3 validates the proposed scheme by comparing numerical results against the PKN
126 solution in the leakoff-dominated regime. In Section 4 we build a 3D field-scale model, loosely
127 based on the In Salah Project and reveal complex interplays between hydraulic fracturing and
128 thermo-poroelastic effects induced by cold CO₂ injection. Section 5 discusses the effects of
129 various reservoir conditions in the context of CGS, on the controlling mechanisms of the growth
130 of caprock fracture. In the concluding section, we suggest possible implications of the proposed
131 method and findings for GCS site characterization and operation.

132 **2 Methodology**

133 In this section, we briefly describe the governing equations of the coupled THM processes taking
134 discrete hydraulic fractures into account. Next, we introduce the coupling scheme that links the
135 coupled THM model to a fracture mechanics module in a simple yet accurate fashion. Note that
136 the THM model used here is an extension of the continuum based THM model as described in
137 Fu et al. (2020). More details related to that THM model, such as derivation of governing

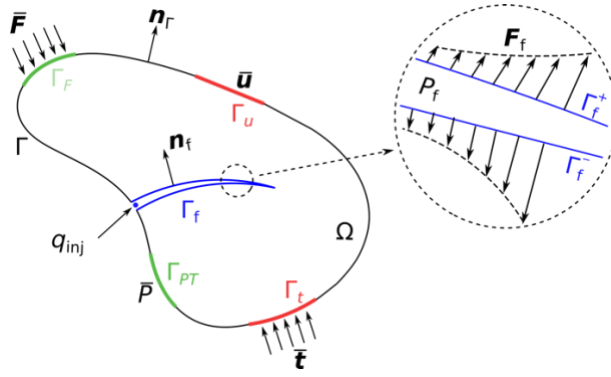
138 equations of multiphase multicomponent flow and heat transfer, numerical discretization, and
139 fixed-stress iterative scheme, can be found in Fu et al. (2020). Moreover, the detailed
140 implementation of the fracturing module used in this study can be found in Fu et al. (2013) and
141 Settgest et al. (2017).

142

143 **2.1 Governing equations of the THM model**

144 As presented in Fig.1, we consider a permeable body Ω bounded by the external boundary Γ that
145 contains Dirichlet and Neumann boundary conditions for geomechanical (traction boundary Γ_t
146 and displacement boundary Γ_u) and flow problems (prescribed pressure/temperature boundary
147 Γ_{pT} and flux boundary Γ_F), respectively. Specifically, for the geomechanical problem, Γ is
148 subjected to the prescribed traction $\bar{\mathbf{t}}$ and displacement $\bar{\mathbf{u}}$ applied on Γ_t and Γ_u , respectively. For
149 the flow problem, prescribed thermodynamic conditions such as pressure \bar{P} , and fluxes of mass
150 or heat ($\bar{\mathbf{F}}$) are applied on Γ_{pT} and Γ_F , respectively.

151 Domain Ω also contains an internal boundary Γ_f , where boundary conditions corresponding to a
152 growing fluid-driven fracture in response to the injected mass q_{inj} are applied. Γ_f describes the
153 fracture whose unit direction vector \mathbf{n}_f is orthogonal to Γ_f and consists of two opposing surfaces
154 Γ_f^+ and Γ_f^- as shown in Fig.1. The body is assumed to be permeable so that leakage \mathbf{F}_f can occur
155 from the fracture to the surrounding body through Γ_f if a positive pressure difference from the
156 fracture to the body is present or vice versa. Note that the process of leakoff is illustrated in the
157 enlarged inset in Fig.1.



158

159 Fig. 1. Conceptual schema for modeling the evolution of a fluid-driven fracture in a permeable medium. Ω is a
 160 permeable body with an external boundary Γ that contains Dirichlet and Neumann boundary conditions for both
 161 geomechanical and flow problems. The evolving fracture in response to the injection fluid of q_{inj} is represented as an
 162 internal boundary Γ_f , highlighted in blue. The enlarged inset illustrates the leakoff of fluids F_f in the fracture through
 163 Γ_f .

164 The reservoir rock and the overlaying/underlying rocks (both caprock and basement) are treated
 165 as porous media subjected to fluid/heat flow as well as poromechanical deformation. The
 166 mathematical formulations and discretization strategy of the THM model are based on the
 167 following set of assumptions and treatments.

- 168 • For the fluid flow and heat transfer model, the movements of mobile phases through
 169 fractures and matrix are assumed to follow lubrication theory (Witherspoon et al., 1980)
 170 and Darcy's law, respectively.
- 171 • For the geomechanical model, the deformation of porous rock matrix is assumed to be
 172 quasi-static and linearly elastic. We use the small deformation assumption for the stress-
 173 strain relationship.
- 174 • Fractures and porous matrix are represented using separate but associated meshes:
 175 Fractures are represented with planar elements in the 3D space while the matrix is

176 represented with solid elements. A mapping between the two meshes is generated as the
177 solid mesh is split to create the fracture mesh.

178 Additional assumptions and treatments associated with multiphase flow and heat transport model
179 are identical to ones adopted in Fu et al. (2020).

180

181 **2.1.1 Geomechanical model**

182 The governing equations for quasi-static solid deformation of a permeable body Ω can be
183 expressed as

$$185 \quad \nabla \cdot \boldsymbol{\sigma} + \rho_m \mathbf{g} = \mathbf{0} \quad (1)$$

186 where $\nabla \cdot$ is the divergence operator; $\boldsymbol{\sigma}$ is the second-order total stress tensor; \mathbf{g} is the gravity
187 vector; and $\rho_m = \phi \sum_{J=A,G} S_J \rho_J + (1 - \phi) \rho_s$ is the bulk density of matrix, in which subscript J
188 denotes a phase of component in porous media (i.e., the aqueous (A) or gaseous (G) phase), S_J is
189 the saturation of phase J , ρ_s is the grain density, and ϕ is the true porosity, defined as the ratio of
190 the pore volume to the bulk volume in the deformed configuration (Kim et al., 2011).

191 Based on the thermo-poroelasticity theory (Biot 1941; Coussy 2004) and the assumptions of
192 linearly elastic and small deformation, $\boldsymbol{\sigma}$ can be related to the temperature field and displacement
193 field:

$$195 \quad \boldsymbol{\sigma} = \mathbf{C}_{dr} : \nabla \mathbf{u} - b P_E \mathbf{1} - 3\alpha_L K_{dr} dT \mathbf{1} \quad (2)$$

194

196 where \mathbf{C}_{dr} is a fourth-order elastic tensor, associated with the drained-isothermal elastic moduli;
 197 ∇ is the gradient operator; \mathbf{u} is the solid displacement vector, also the primary unknown of the
 198 geomechanical model; b is Biot's coefficient; $\mathbf{1}$ is a second-order identity tensor; α_L is the linear
 199 coefficient of thermal expansion; K_{dr} is the drained-isothermal bulk modulus; $P_E = \sum_J S_J P_J -$
 200 $\int_{S_A}^1 P_c(S) dS$ is the equivalent pore pressure (Coussy 2004), in which P_J is the fluid pressure of
 201 phase J and P_c is the gas-water capillary pressure as a function of aqueous saturation; and $dT =$
 202 $T - T_{ref}$ is the temperature difference, in which T is the current temperature and T_{ref} is a
 203 reference temperature.

204 In the geomechanical model, we consider the fluid pressure in the fracture, P_f , as a normal
 205 traction exerted on the fracture faces, Γ_f , while we neglect the shearing traction of the fluid on
 206 solid matrix. Therefore, the traction balance across the fracture surface can be written as

$$207 \quad \mathbf{t}_f = -P_f \mathbf{n}_f \text{ on } \Gamma_f \quad (3)$$

208 The external boundary conditions, traction and kinematic, are governed by

$$209 \quad \bar{\mathbf{t}} = \boldsymbol{\sigma} \mathbf{n}_t \text{ on } \Gamma_t, \quad (4)$$

$$210 \quad \bar{\mathbf{u}} = \mathbf{u} \text{ on } \Gamma_u, \quad (5)$$

211 Where \mathbf{n}_f and \mathbf{n}_t are the normal unit vectors on Γ_f and Γ_t , respectively; $\bar{\mathbf{u}}$ is the prescribed
 212 displacement on Γ_u .

213

214 **2.1.2 Multiphase multicomponent flow and heat transfer model**

215 The formulations of mass-and-energy conservation can be expressed in a unified
 216 integrodifferential form as:

217
$$\frac{d}{dt} \int_{\Omega_\alpha} M_\alpha^\kappa d\Omega_\alpha + \int_{\Gamma_\alpha} \mathbf{F}_\alpha^\kappa \cdot \mathbf{n} d\Gamma_\alpha = \int_{\Omega_\alpha} q_\alpha^\kappa d\Omega_\alpha, \quad \kappa \equiv c, w, \theta; \quad \alpha \equiv m, f$$

218 (6)

219 where subscript α denotes a type of flow model (i.e., matrix flow model when $\alpha = m$, and
 220 fracture flow model when $\alpha = f$); superscript κ denotes a component (i.e., CO₂ when $\kappa = c$, and
 221 water when $\kappa = w$) or heat (when $\kappa = \theta$) in porous media, respectively.

222 For the matrix flow model ($\alpha = m$), the formulation is identical to the one given by Fu et al.
 223 (2020). For the fracture flow model ($\alpha = f$), the mass accumulation term M_f^κ integrating over an
 224 arbitrary volume of a fracture is given by:

225
$$M_f^\kappa = \int_{\Gamma_f} \sum_{J=A,G} S_J \rho_J X_J^\kappa w^h d\Gamma_f$$

226 (7)

227 where X_J^κ is the mass fraction of component κ in phase J and ρ_J is the density of phase J . The
 228 volume of a fracture Ω_f is assumed to be the integral of the product between its surface area Γ_f
 229 and hydraulic aperture w^h , represented by the gray volume in Fig. 2(a), which can be expressed
 230 as:

232
$$w^h = (\mathbf{u}^+ - \mathbf{u}^-) \cdot \mathbf{n}_f$$

231 (8)

233 where $\mathbf{u}^+ - \mathbf{u}^-$ is the discontinuity in the displacement field across Γ_f . Eq. (8) provides a direct
 234 coupling between the displacement field and the fracture flow.

235 Employing the assumption of the lubrication theory for fluid flow in fractures yields the mass
 236 fluxes term of different components, \mathbf{F}_f^κ , expressed as

$$237 \quad \mathbf{F}_f^\kappa = - \sum_{J=A,G} \rho_J X_J^\kappa \frac{(w^h)^2}{12\mu_J} \nabla P_J$$

238 (9)

239 where μ_J denotes the dynamic viscosity of fluid in phase J ; ∇P_J is the fracture pressure gradient
 240 in phase J . All mass-and-heat fluxes through a fracture surface are determined via looping
 241 through its edges and summing fluxes from its neighboring surfaces. The transmissivity between
 242 fracture surfaces of different aperture is computed following the treatment given in Pruess and
 243 Tsang (1990). The mass-and-heat fluxes due to leakoff processes (as illustrated in the inset of
 244 Fig.1) can be written, using Darcy's law by assuming a Newtonian flow, as:

$$246 \quad \mathbf{F}_\alpha^\kappa = - \sum_{J=A,G} \rho_J X_J^\kappa \frac{k_J^f}{\mu_J} \mathbf{k} (\nabla P_J - \rho_J \mathbf{g})$$

245 (10)

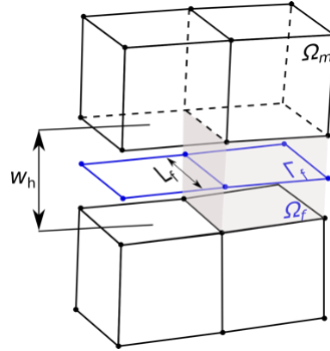
247 where \mathbf{k} is the intrinsic permeability tensor of matrix elements adjacent to a fracture face. Eq.
 248 (10) shows the transmissivity of the leakoff term principally depends on the hydraulic properties
 249 of the matrix elements and the corresponding leak-off area is equal to Γ_f .

250 For the component of water in the aqueous phase, the Dirichlet (in terms of fluid pressure \bar{P}) and
 251 Neumann boundary conditions (in terms of mass flux $\bar{\mathbf{F}}$) for the coupled thermo-hydro problem
 252 can be expressed as follow:

$$253 \quad \bar{\mathbf{F}} = \mathbf{F}_\alpha^w \mathbf{n}_F \text{ on } \Gamma_F, \quad (11)$$

$$254 \quad \bar{P} = P_A \text{ on } \Gamma_{PT}, \quad (12)$$

255 where \mathbf{n}_F is the normal unit vectors exerted onto Γ_F ; Γ_F and Γ_{PT} are the fixed mass flux and fluid
 256 pressure boundaries in the matrix, respectively.



257
 258 Fig. 2 Illustration of spatial discretization for coupled fracture-matrix flow model. Simulation domains of fracture
 259 are displayed in blue, matrix domains in gray.

260

261 2.1.3 Thermo-poromechanics

262 We employ the fixed-stress iterative scheme to solve thermo-poromechanics in rock matrix (Kim
 263 et al., 2011). In this scheme, the coupled THM problem splits into two subproblems, i.e. a fluid-
 264 heat flow problem and a geomechanical problem. During each iteration, the subproblems are
 265 solved in an iterative sequence until the convergence of both problems. Particularly, in solving
 266 the fluid-heat flow problem, the current true porosity is estimated from its previous state with the
 267 following equation and assuming the rate of total volumetric stress remain unchanged throughout
 268 the current time step.

$$270 \quad d\phi = \frac{b - \phi}{K_{dr}} (dP_E + d\sigma_v) + 3\alpha_L b dT \quad (13)$$

269

271 where σ_v is volumetric total stress.

272 The numerical treatment of implementing the fixed-stress iterative scheme follows the same
273 procedure described in Fu et al. (2020).

274

275 **2.1.4 Fracture mechanics module**

276 We adopt the fracture mechanics module of GEOS, a high-performance computing simulation
277 code (Fu et al. 2013; Settgast et al. 2016; Ju et al., 2020), to simulate fracture propagation. This
278 module uses linear elastic fracture mechanics and a modified virtual crack closure technique
279 (MVCCT) to calculate energy release rate G at the fracture tip (Huang et al., 2019). The fracture
280 extends from the tip into intact rock when G exceeds the critical value G_c , which can be related
281 to the critical stress intensity factor K_{Ic} , also known as fracture toughness, through

$$283 \quad G_c = K_{Ic}^2 \left(\frac{1 - \nu^2}{E} \right) \quad (14)$$

284 When fracturing occurs, new fracture faces are created by splitting the nodes between the two
285 solid elements adjacent to the tip faces. As mentioned in the previous section, the fluid pressure
286 along the fracture is applied to the solid elements that are connected with those faces via a
287 normal traction force. Properly implementing this traction boundary condition is essential for
288 satisfying the momentum balance of solid elements in the updated mesh topology. Moreover, the
289 fluid-heat flow in newly created faces are automatically integrated into the matrix-fracture flow
290 system, ensuring mass-and-energy balance across the entire domain.

291 **2.2 The coupling scheme between the THM model and fracture mechanics module**

292 The three main components of our model, (1) the multiphase multi-component solver for porous
293 medium and fracture flow, (2) the hydraulic fracturing module, and (3) the poromechanics

294 solver, are all known to face their own numerical challenges (Kim and Moridis 2013; Settgest et
295 al., 2016; White et al., 2016). These modules are challenging even under less challenging
296 conditions, namely without the complication of fracturing for the first component and when the
297 latter two only deal with single-phase flow. In prior works, we have developed relatively robust
298 individual modules on a common platform, GEOS, for these three components (Settgest et al.,
299 2016; Fu et al., 2020). Still, coupling these three components together is a challenging task.

300 It is widely acknowledged that an implicit coupling strategy theoretically provides
301 unconditionally convergent numerical solutions and enables large timesteps for the preceding
302 coupled problem (Kim et al., 2012; Girault et al., 2016). However, the actual implementation to
303 implicitly couple the three aforementioned modules faces practically insurmountable numerical
304 difficulties, exacerbated by challenges associated with the parallel computing environment. We
305 therefore develop a sequential coupling scheme to take full advantage of existing modules in
306 GEOS. Meanwhile, as sequential coupling often suffers from poor convergence, we capitalize on
307 the inherent self-stabilizing features of leakoff-dominated fracturing to simplify the coupling
308 scheme.

309 In this scheme, we use a compositional reservoir simulator for the fluid-heat flow problem and a
310 standard Galerkin finite element method for geomechanics. As mentioned in section 2.1.4, the
311 fracture mechanics module evaluates the fracturing criterion as well as updates the solid mesh
312 and flow network once new fracture surfaces are generated. The sequential communication
313 between the THM model and fracture mechanics module is achieved by sharing key information,
314 such as fluid pressure in fractures and displacement fields, at every timestep (see Fig. 3). This
315 procedure can be performed without compromising the modularity of the code because only
316 minor modifications are required for existing individual modules.

317 The relationships among the physical processes involved in the problem are summarized in
318 Table 1. Several interactions have been implicitly handled in existing modules. For instance, the
319 fracture flow and matrix flow are solved together by unifying the fracture flow network and the
320 matrix flow mesh in a combined flow topology as shown in Fig. 2. In other words, in the cell-
321 centered finite volume framework, both the flow “faces” for fracture flow and the solid
322 “elements” for matrix flow are considered “cells” interconnected together. Also, the solid
323 deformation and matrix flow are already coupled using the “fixed-stress” scheme in the
324 poromechanics solver. The remaining relationships are enforced sequentially as shown in Fig. 3.

325 As we will now explain, an inconsistency and thereby an error are introduced in the coupled
326 solution flow. In the n^{th} iteration of each time step, the aperture is computed in Steps 3 and 4 (see
327 Fig. 3) based on the geomechanical module’s results. In iteration $n+1$ ’s Step 1, the initial “guess”
328 of the fracture cells’ states is based on the solved pressure from Step 1 and the aperture from
329 Steps 3 – 4 of iteration n . Therefore, the aperture update in iteration n would introduce a small
330 extra (positive or negative) fluid mass to the system. We found this treatment is greatly
331 beneficial for the convergence of the solution for the following reason. An open fracture’s
332 aperture is extremely sensitive to fluid pressure. If we use the fluid mass in each fracture cell
333 from iteration n ’s Step 1 while using the updated aperture, the initial “guess” of the flow
334 system’s state in iteration $n+1$ would be highly volatile and usually far from the “true” solution,
335 resulting in severe convergence difficulties. We hypothesize that the fluid mass inconsistency is
336 inconsequential for the overall accuracy of the solved system because only a very small fraction
337 of the injection fluid is stored in the fracture, a salient feature of the leakoff-dominated regime.

338 In the verification solution in Section 3 and simulation results in Section 4, we compare the total
339 masses of CO₂ in the numerical models with the total injected quantities to quantify the induced

340 error. Note that rock porosity is not very sensitive to pressure change, so this treatment is
 341 unnecessary for the rock matrix cells.

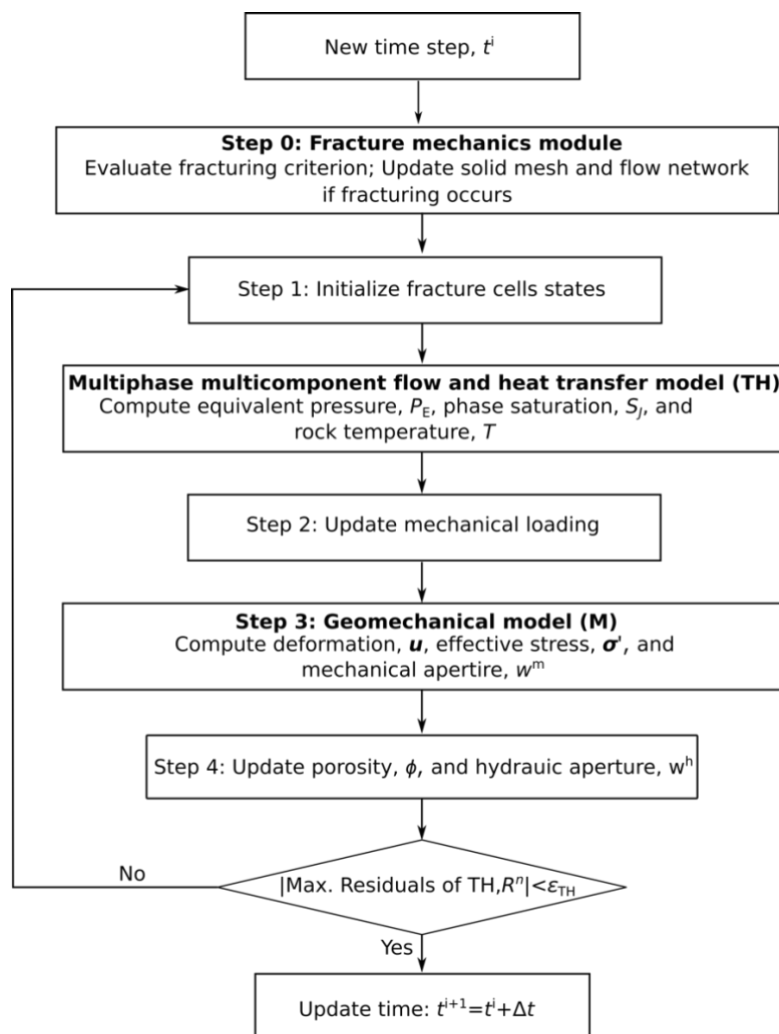
342 Table 1. Coupling relationships between individual modules. The “step” in each cell refers to an “operation” in the
 343 flow diagram in Fig. 3 where the interaction is embodied.

Modules providing information	Modules receiving information			
	Fracture Flow	Matrix flow	Solid deformation	Fracture mechanics
Fracture Flow	Self	Pressure boundary condition along fracture faces; solved together.	Traction boundary condition along fracture faces. Step 2.	Indirect influence, through solid deformation
Matrix flow	Fluid leakoff; solved together	Self	Solved together in poromechanics	Indirect influence, through solid deformation
Solid deformation	Hydraulic aperture and fluid storage. Step 4.	Solved together in poromechanics	Self	Compute energy release rate. Step 0.
Fracture mechanics	New fracture flow elements. Step 0.	Indirect influence, through fracture flow	Updated mesh. Step 0.	Self

344

345 We found the sequential coupling scheme to have satisfactory numerical performance: Most time
 346 steps converge within five iterations; The scheme is stable provided the time step is significantly
 347 smaller than the time that it takes the fracture to propagate the distance of one-element length.

348 This is again largely owing to the self-stabilizing features of fracture propagation in the leakoff-
 349 dominated regime: As the permeability of the reservoir is largely constant, the leakoff rate is
 350 mostly determined by the difference between fluid pressure in the fracture and the far-field fluid
 351 pressure in the reservoir. In a propagating fracture, the fluid pressure is always marginally higher
 352 than the “fracture propagation pressure”, which, in the scenarios concerned by this study, is
 353 approximately the “fracture opening pressure” near the fracture front. The fracture opening
 354 pressure is in turn determined by the total stress in the system, which evolves very slowly.
 355 Therefore, a convergent numerical solution can be obtained as long as the effects of the
 356 extending fracture surface area on the flow into the rock matrix are captured.



358 Fig. 3. Flowchart of the coupling scheme between coupled THM coupled model and fracture mechanics module.
359 The coupling convergence criterion of coupled THM model is that the maximum residuals of TH model is smaller
360 than ε , a pre-set small value, say 10^{-5} , after updating perturbed hydraulic variables.

361 **3 Verification**

362 In this section, we compare the new model's results with the PKN solution in the leakoff-
363 dominated regime to verify the numerical implementation of the model and, particularly, to
364 validate the coupling scheme presented in Section 2.2.2. Note that the validation of relevant
365 individual submodules in GEOS has been reported in previous works, in which numerical results
366 are compared with the analytical solutions of poromechanics (Terzaghi's and Mandel's problems
367 (Fu et al., 2019; Fu et al., 2020)), and of fracturing propagation in different regimes (Fu et al.,
368 2013; Settgest et al., 2017).

369

370 **3.1 The PKN solution in the leakoff-dominated regime**

371 We use a standard fracture geometry, the PKN model as illustrated in Fig. 4(a), to test the
372 proposed coupling scheme (Perkins and Kern 1961; Nordgren 1972). The origin of the
373 coordinate system is set at the injection point; the x -direction coincides with the fracture
374 propagation direction, so the y -axis is along the direction of the minimum principal *in situ* stress
375 S_{hmin} . Recall that hydraulic fracturing in a storage reservoir with moderate permeability is in the
376 leakoff-dominated regime. We therefore compare the numerical solutions against the PKN model
377 in the so-called leakoff-dominated regime (Nordgren 1972). This solution describes the growth
378 of a fixed-height vertical fracture when the volume of fluid loss into the reservoir is much larger
379 than the volume stored in the fracture.

380 According to the analytical solution (Nordgren 1972), the half fracture length L_f and aperture w_0^h
381 at the wellbore are

$$L_f = \frac{qt^{1/2}}{2\pi C_L h_f} \quad (15)$$

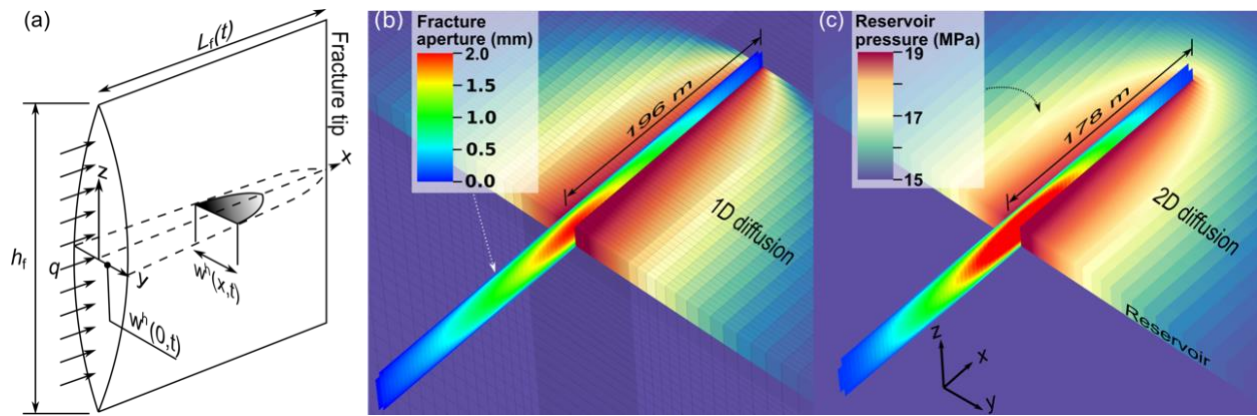
$$w_0^h = 4 \left[\frac{\mu q^2}{\pi^3 E' C_L h_f} \right]^{1/4} t^{1/8} \quad (16)$$

386 where q is the total injection rate; h_f is the fracture height; $E' = E/(1-\nu^2)$ is the plane-strain
387 modulus for the formation; and C_L is the Carter's leakoff coefficient. As revealed in Howard and
388 Fast (1957), C_L can be expressed as:

$$C_L = \Delta P \left(\frac{k_r \phi c_t}{\pi \mu} \right)^{1/2} \quad (17)$$

391 where ΔP is the difference between the fracture pressure and the remote reservoir pressure that is
392 assumed to be constant; k_r is the intrinsic permeability of the reservoir; and $c_t = c_f + c_p$ is the total
393 compressibility, where c_f is fluid compressibility and c_p is pore compressibility, both of which
394 are constants in equation (17). However, in a high-fidelity numerical model, c_f and c_p
395 respectively depend on the nonlinear PVT properties of fluids and the solid deformation in the
396 coupled THM models. Therefore, when applying the analytical solution, we set c_t to the value
397 computed from the numerical models for simplicity. Also note that equation (17) assumes 1D
398 diffusion, which is not necessarily valid in a real reservoir or in a high-fidelity numerical model.

399 Some additional, special adaptations of the numerical model are needed to be consistent with
 400 assumptions of the analytical solution. The analytical solution intrinsically assumes zero
 401 toughness for the reservoir rock. Accordingly, we set the toughness of reservoir rock to
 402 $100 \text{ Pa}\cdot\text{m}^{0.5}$, a small finite value that prevents small numerical noise from triggering fracturing
 403 artificially. The analytical solution calculates leakoff using Carter's leakoff coefficient, which is
 404 based on 1D diffusion. However, the fluid flow in the THM coupled model is 3D in nature. To
 405 match the 1D diffusion assumption, we use a strongly anisotropic permeability ($k_{ry}=10 \text{ mD}$,
 406 $k_{rx}=k_{rz}=0 \text{ mD}$). We also run an additional simulation by removing the 1D diffusion restriction for
 407 comparison. Moreover, the Biot coefficient is set to zero in the numerical model, since the PKN
 408 model does not incorporate the poromechanical effects in the reservoir. Note that none of the
 409 above adaptations is used in the 3D simulations in section 4 and beyond.



410
 411 Fig. 4. Geometrical characteristics (a) and simulation results for a PKN fracture with $q=0.04 \text{ m}^3/\text{s}$ in the case of (b)
 412 1D diffusion and (c) 2D diffusion at $t=4\times 10^5 \text{ s}$. In (a) where only one wing of the fracture is shown due to symmetry,
 413 h_f , q , w^h , and L_f indicate fracture height, injection rate, fracture width (aperture), and fracture length, respectively. In
 414 (b) and (c), a full length/height of the fracture and a quarter of the reservoir pressure field are presented. Note that
 415 fracture color scale indicates fracture aperture, whereas the color scale for the matrix indicates reservoir pressure.

416 3.2 Numerical realization of the PKN model

417 The numerical simulation only models one quarter of the problem owing to the symmetrical
418 condition of PKN model, as shown in Fig. 4(a). To minimize boundary effects, the dimensions of
419 the quarter model are 1000 m, 2000 m, and 1000 m in x -, y -, and z -directions, respectively,
420 where meshing in each dimension contains a refined portion (200 m, 100 m, and 40 m in x -, y -,
421 and z -directions, respectively) and coarse portion. The refined region uses constant mesh
422 resolutions in three directions, i.e. 4 m, 1 m, and 2 m, respectively, whereas the coarse region
423 uses a progressively coarser mesh resolution toward the far-field. The model is discretized into
424 1,004,731 hexagonal elements. We simulate fracture propagation and reservoir response for three
425 different injection rates as listed in Table 1. The fourth simulation removes the 1D diffusion
426 restriction for the baseline injection rate and results are denoted by “2D diffusion” in Fig. 4 and
427 5. Parameters adopted in the verification are listed in Table 1.

428

429 Table 1. Parameters employed in the numerical model for the simulation of the PKN model.

Property	Value
Fracture height, H_f	40 m
Injection rate, q	0.02, 0.04 ^a , and 0.06 m ³ /s
Dynamic viscosity, fluid, μ	1×10^{-3} Pa s
Porosity, ϕ	0.2
Pore compressibility, c_t	1.04×10^{-8} Pa ⁻¹
Poisson's ratio, ν	0.25
Biot's coefficient, b	0.0
Carter's leakoff coefficient, C_L	0.493 mm/ \sqrt{s}
Young's modulus, E	10 GPa
Critical stress intensity factor (toughness), reservoir	100.0 Pa•m ^{0.5}

430 ^abaseline case simulation

431

432 **3.3 Verification results**

433 Fig. 5 shows a comparison of results from the numerical simulation and the PKN solutions. In
434 general, the temporal evolution of fracture length for the three injection rates are in good
435 agreement with the corresponding analytical solutions. The numerically simulated apertures tend
436 to deviate from the analytical solutions early in the injection but gradually converge to the
437 solutions as injection progresses.

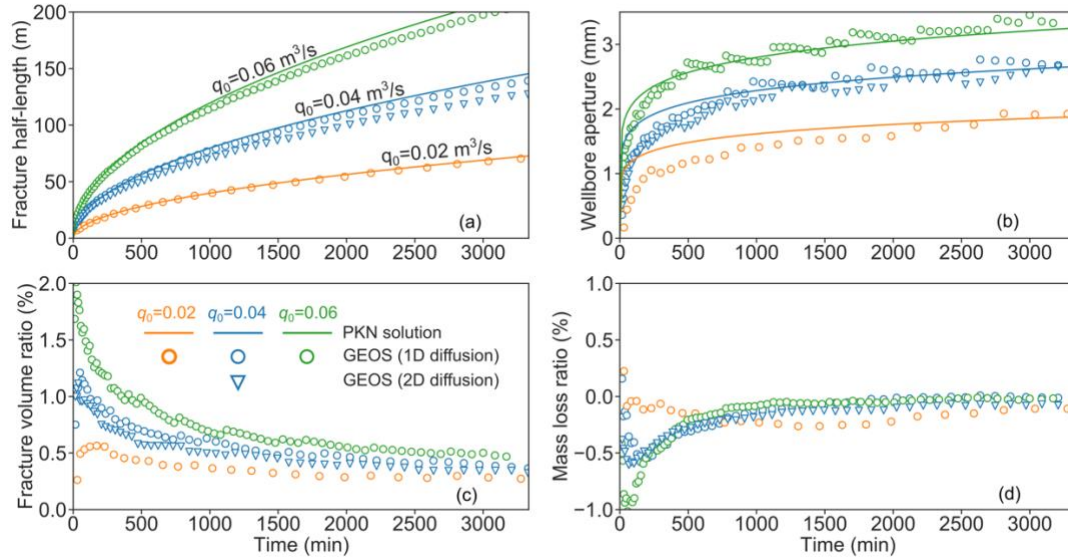
438 The disparity between the numerical solution and the PKN solution at the early times is likely
439 caused by the geometric assumptions of the PKN model, i.e. the fracture length being much
440 larger than the fixed fracture height (a rectangular fracture shape). In the early stage of injection,
441 the fracture length simulated by the numerical model, however, is smaller than or similar to the
442 preset fracture height, forming a penny shape and therefore a direct comparison between
443 solutions with different fracture shape assumptions is not appropriate. Note that for all the three
444 injection rates, the numerically predicted apertures become very similar to the analytical
445 solutions when the half fracture length in each case reaches around 200 m, 2.5 times the fracture
446 height. Fig. 5(b) also shows that numerical results of wellbore aperture exhibit a moderate
447 oscillatory behavior. This behavior is expected because the spatial discretization scheme dictates
448 that the fracture has to propagate by the length of an element, yielding numerical
449 overshoot/undershoot.

450 As shown in Fig. 5(c), the percentage of fluid in the fracture compared with the total injection
451 volume, termed “*fracture volume ratio*” in this study, is quite low, generally less than 1%. This
452 confirms that these four simulated hydraulic fractures are indeed in the leakoff-dominated
453 regime. Note that the “*fracture volume ratio*” is mathematically identical to the “*fluid efficiency*”

454 used in unconventional reservoir stimulation. However, we avoid using this established term
455 because in carbon storage, retaining more fluid in the fracture, i.e. achieving a “high fluid
456 efficiency”, is not an objective.

457 Fig. 5(d) shows the temporal evolution of “*mass loss ratio*”, defined as the percentage of mass
458 loss induced by the coupling scheme compared with total injection mass in this study. Note that a
459 negative mass loss ratio means extra masses are introduced in the system. A small yet noticeable
460 error is introduced at early time by the inconsistency in the coupling scheme. However, this
461 inconsistency rapidly diminishes, and the absolute mass losses converge to near 0.05 % as the
462 leakoff dominates. The convergence of mass loss ratio for each case validates our hypothesis that
463 the mass loss induced during the coupling is indeed trivial and proves the accuracy of our
464 coupling scheme for simulating leakoff-dominated fracturing.

465 The comparison between Fig. 4(b) and (c) shows the fracture length grows faster in the case of
466 1D diffusion than that of 2D diffusion where the reservoir pressure plume front goes farther than
467 the crack tip. Likewise, Fig.5 (a) and (c) shows that the case of 2D diffusion yields a slightly
468 higher leakoff compared with the baseline verification (1D diffusion), which includes lower
469 fracture growth rate and smaller wellbore aperture. Those behaviors are mainly owing to the
470 overestimation of the actual C_L when 2D diffusion is invoked (Carrier and Grant, 2010; Fu et al.,
471 2017).



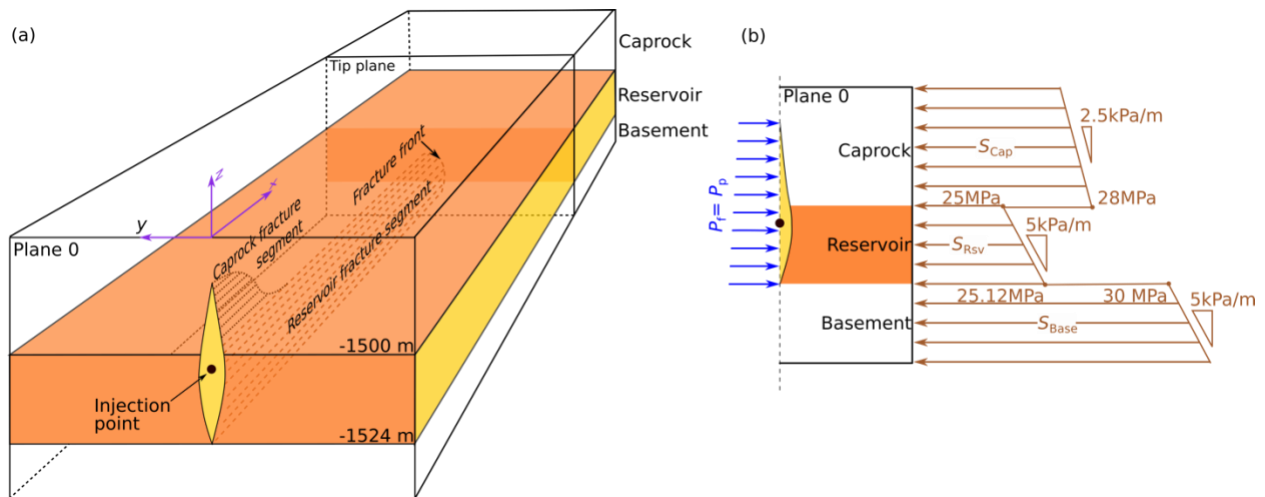
472

473 Fig. 5. Simulation results for a PKN fracture in the leakoff-dominated regime. (a), (b), (c) and (d) plot the temporal
 474 variations of fracture half-length, wellbore aperture, fracture volume ratio, and mass loss ratio respectively.

475 Analytical solutions for leakoff-dominated fractures are plotted in (a) and (b) for comparison. The fracture volume
 476 ratio in (c) denotes the percentage of the total injected fluid stored in the fracture. The mass loss ratio in (d) denotes
 477 the percentage of the mass loss induced by the coupling scheme compared with the total injection mass.

478 **4 Application in simulating fracturing into caprock**

479 To demonstrate the capabilities of the proposed scheme and apply it to GCS, we build and
 480 analyze a field-scale 3D numerical model (hereafter referred to as the baseline case) in GEOS in
 481 this section. The baseline model is loosely based on the geological settings of the In Salah
 482 storage site (Rutqvist et al., 2010; Ringrose et al., 2013; White et al., 2014), as shown in Fig. 6
 483 (a), while the analyses generally apply to a GCS reservoir with marginal permeability.



484

485 Fig. 6. (a) 3D schematic (not to scale) of the configuration, geometry and dimensions of the baseline model showing
 486 one wing of a hydraulic fracture penetrating into the caprock, with cold supercritical CO₂ entering the computational
 487 domain from the injection point, marked as a black dot on the plane 0 ($x=0$). Tip plane tracks the movement of
 488 fracture front. Sub-figure (b) shows internal and external traction boundary conditions, i.e. fracture pressure and
 489 horizontal *in-situ* stress, applied to the 3D model on plane 0. Note that only one wing of the fracture in panel (a) is
 490 shown due to symmetry.

491

492 4.1 Model setup

493 Fig. 6(a) schematically depicts the 3D geometry of the baseline model. The CO₂ storage
 494 reservoir of marginal permeability is sandwiched between the caprock and the basement, both of
 495 which are much less permeable. The reservoir is 24 m thick with its interface with the caprock
 496 located at 1500 m depth ($z = -1500$ m). We established a 3D coordinate system, in which the x -
 497 axis is parallel to the direction of the maximum *in situ* horizontal stress (S_{Hmax}), the y -axis is
 498 parallel to the direction of minimum *in situ* horizontal stress (S_{Hmin}), the z -axis points upward,
 499 and the origin at ground surface resides above the injection point. The injection point is
 500 annotated as a black dot in Fig.6 (a) to highlight its position. Note that the vertical location of the
 501 injection point should not alter the outcome of fracturing because there is no fracturing barrier

502 inside the reservoir. The initial pore pressure follows the hydrostatic distribution and the initial
503 reservoir temperature is set as 65 °C. The minimum principal *in situ* stress (S_{hmin}) follows a
504 segmented-linear distribution along the z direction, as shown in the right portion of Fig. 6(b).
505 S_{hmin} spatial distributions with caprock, reservoir, and basement layers are denoted by S_{Cap} ,
506 S_{Rsv} , and S_{Base} , respectively. We assume that there is a fracturing barrier between the reservoir
507 and basement that prevents downward fracturing as we mainly focus on conditions and
508 mechanisms for fracturing in the reservoir and caprock. As illustrated in Fig. 6(a), the fracture
509 propagation is assumed to only take place within the x - z plane, perpendicular to the direction of
510 S_{hmin} . Note that the symmetry of the system with respect to the y - z plane at the injection point
511 allows the use of a half model.

512 Fully-saturated supercritical CO₂ at an injection temperature of 45°C, is injected into the
513 reservoir at a constant rate of 15.0 kg/s (one wing of fracture), approximately a million metric
514 ton per year. We assume that the injection well is cased, and fractures are initiated from
515 perforations, which limits the well only to communicate with the system through the fracture.
516 Thus, the injection well can be simplified as a point source in our 3D computational domain. The
517 so-called “roller” boundary condition is applied to all “far-field” boundaries of the
518 geomechanical model. For the fluid flow model, prescribed mass/heat rate conditions for the
519 injection well are applied at $x=0$, $y=0$ and $z=-1504$ m. We apply the original reservoir pressure
520 and a constant ambient temperature (65°C) at the lateral boundaries as the far-field Dirichlet
521 boundary conditions. No-flow conditions are applied to elements on the top and bottom planes.
522 The computational domain of the baseline case has a core region whose dimensions in x -, y -, and
523 z -directions are 800 m, 200 m, and 240 m, respectively. The core region has a relatively fine
524 mesh resolution of 8.0, 4.0, and 8.0 m in those directions. Surrounding the core region is a

525 coarsely resolved region that extends to 5800 m, ± 9000 m, and ± 400 m in the respect three
526 directions, which mitigates boundary effects while maintaining computational efficiency. The
527 baseline model involving a kilometer-scale reservoir and 3 years of injection time, is discretized
528 into 1,344,000 elements and the simulation is conducted across 252 CPU cores (16 Intel®
529 Xeon® E5-2670 CPUs), which runs for 18 hours on a high-performance computer (4536 core-
530 hours in total).

531 Table 3 summarizes the computational parameters and constitutive models for the baseline
532 model. As for the mobility-related constitutive models in multiphase flow model, we use a
533 Corey-type relative permeability functions (Brooks and Corey, 1964) and a van Genuchten
534 capillary function (Van Genuchten, 1980), respectively written as Eq. (18) and (19).

$$535 \quad k_A^r = S_n^4, k_G^r = (1 - S_n)^2(1 - S_n^2) \quad (18)$$

$$536 \quad P_c = -P_0[(S^*)^{-1/\lambda} - 1]^{-1/\lambda}, S^* = (S_A - S_{irA})/(1.0 - S_{irA}) \quad (19)$$

537 where k_A^r and k_G^r are relative permeabilities in aqueous and gaseous phases; $S_n = (S_A -$
538 $S_{irA})/(1.0 - S_{irA} - S_{irG})$ is the normalized aqueous saturation; S_{irA} and S_{irG} are the irreducible
539 aqueous saturations and the residual gas saturations, respectively. λ and P_0 are the exponent that
540 characterizes the capillary pressure curve and the capillary modulus, respectively. Then, we set
541 $S_{irA} = 0.12$ and $S_{irG} = 0.01$ for relative permeability, and $S_{irA} = 0.11$, $P_0 = 12500$ Pa, and $\lambda =$
542 0.254 for capillarity, where the capillary pressure model employs a slightly smaller S_{irA} than the
543 model of relative permeability in order to prevent unphysical behavior (Moridis and Freeman,
544 2014).

545

546 Table 2. Parameters employed in the baseline simulation

Property	Baseline value
Reservoir thickness, H_r	24 m
Minimum principal <i>in situ</i> stress in reservoir, total stress, mid-depth, S_{hmin}^r	25 MPa
Minimum principal <i>in situ</i> stress in caprock, total stress, mid-depth, S_{hmin}^c	30 MPa
Initial pore pressure, mid-depth of reservoir, P_{int} (hydrostatic condition applies)	15 MPa
Biot's coefficient, reservoir rock, b_r	0.5
Biot's coefficient, caprock, b_c	0.25
Intrinsic permeability, reservoir, k_r	15 mD
Intrinsic permeability, other layers, k_c	0.1 μ D
Porosity, reservoir, ϕ_r	0.15
Porosity, all other layers, ϕ_c	0.05
Young's modulus, all layers, E	10 GPa
Poisson's ratio, all layers (Armitage et al., 2010), ν	0.25
Initial temperature, all layers, T_{int}	65 °C
Coefficient of thermal expansion, linear, α_L	10^{-5} /°C
Injection temperature, T_{inj}	40 °C
Thermal conductivity, all layers, λ	3.0 W/(m·K)
Heat capacity, all layers, C_s	1000 J/(kg·K)
Critical stress intensity factor (toughness), all layers (Senseny and Pfeifle, 1984)	1.0 MPa·m ^{0.5}
Relative permeability model ^a (Brooks and Corey, 1964)	$k_A^r = S_n^4$ $k_G^r = (1 - S_n)^2(1 - S_n^2)$ $S_n = (S_A - S_{irA}) / (1.0 - S_{irA} - S_{irG})$ $S_{irA} = 0.12, S_{irG} = 0.01$

Capillary pressure model ^b (Van Genuchten, 1980)	$P_C = -P_0[(S^*)^{-1/\lambda} - 1]^{-1/\lambda}$ $S^* = (S_A - S_{irA})/(1.0 - S_{irA})$ $S_{irA} = 0.11, P_0 = 12500 \text{ Pa}, \lambda = 0.254$
---	---

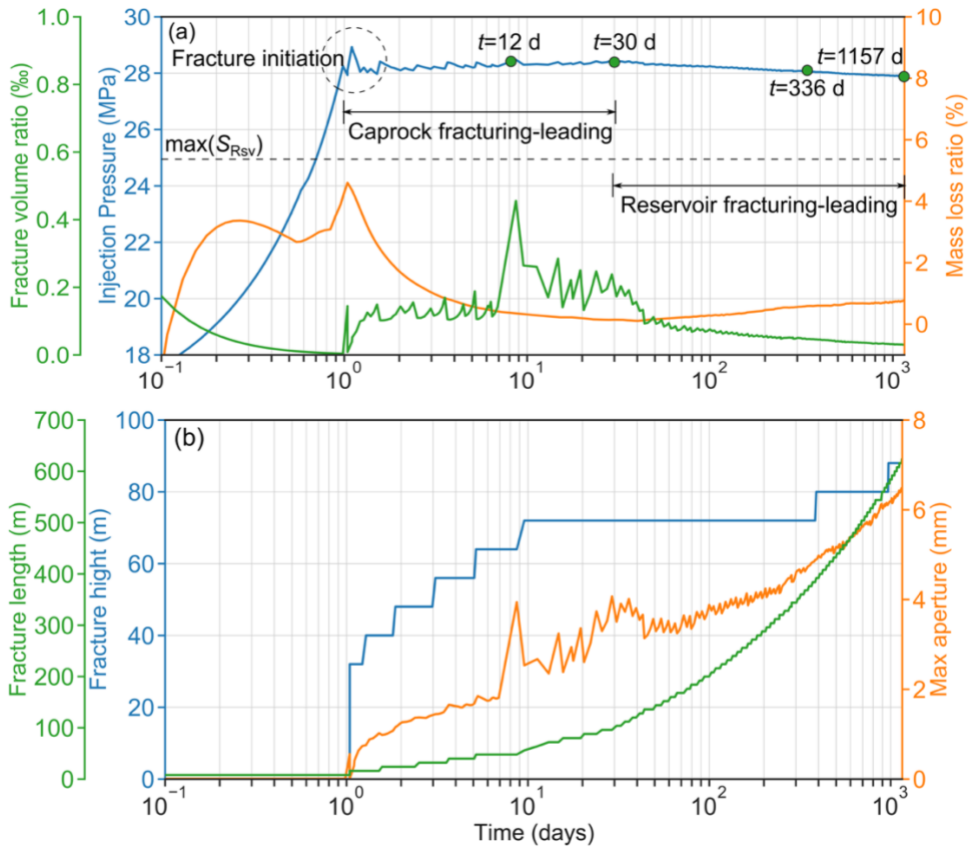
547 a k_A^r and k_G^r are relative permeabilities in aqueous and gaseous phases; S_n is the normalized aqueous saturation; S_{irA}
548 and S_{irG} are the irreducible aqueous saturation and the residual gas saturation, respectively

549 b P_0 is the capillary modulus

550

551 4.2 Results of baseline model

552 As presented in Fig. 7 and Fig. 8, results of the baseline model clearly show how a leakoff-
553 dominated fracture is driven by injection and provides an evolving interface between injection
554 and reservoir storage. By the end of three years of injection, the fracture has propagated 620 m
555 into the reservoir, providing a growing interface plane for feeding injected CO₂ into the
556 reservoir. The CO₂ plume advances approximately 625 m in the y-direction on each side (Fig.
557 8(p)), spanning an area of reservoir as large as about 1.24×1.25 kilometers. Note that the rate of
558 injection employed in the baseline case cannot possibly be achieved if the downhole injection
559 pressure is strictly limited to below the estimated fracturing pressure of the caprock,
560 approximately 25 MPa. Meanwhile, the maximum fracture height only reaches 88 m, thereby
561 being vertically contained in the lower portion of the caprock (Fig. 7(b) and Fig. 8(m)). Note that
562 the containment mechanism will be elucidated in the subsequent analysis.



563

564 Fig. 7. Overall responses of the system in the baseline case. (a) Fracture volume ratio, injection pressure, and mass

565 loss ratio versus time; (b) Fracture length, fracture height, and max aperture versus time. The curve colors in (a) and

566 (b) correspond to their y axes. Fracture volume ratio is the percentage of injected fluid retained in the fracture.

567 Injection pressure is measured at the injection point at the entrance to the fracture. Mass loss ratio is the percentage

568 of injected CO_2 mass that is “lost” due to the error introduced by the sequential iteration scheme as explained in

569 section 3.3. Note that the highest stress level of S_{Rsv} , $\max(S_{Rsv})$, which is the in situ stress magnitude at the bottom

570 of the reservoir, is indicated by a black dash line in (a).

571

572 Another interesting observation is the evolution of injection pressure (the blue line in Fig. 7(a))

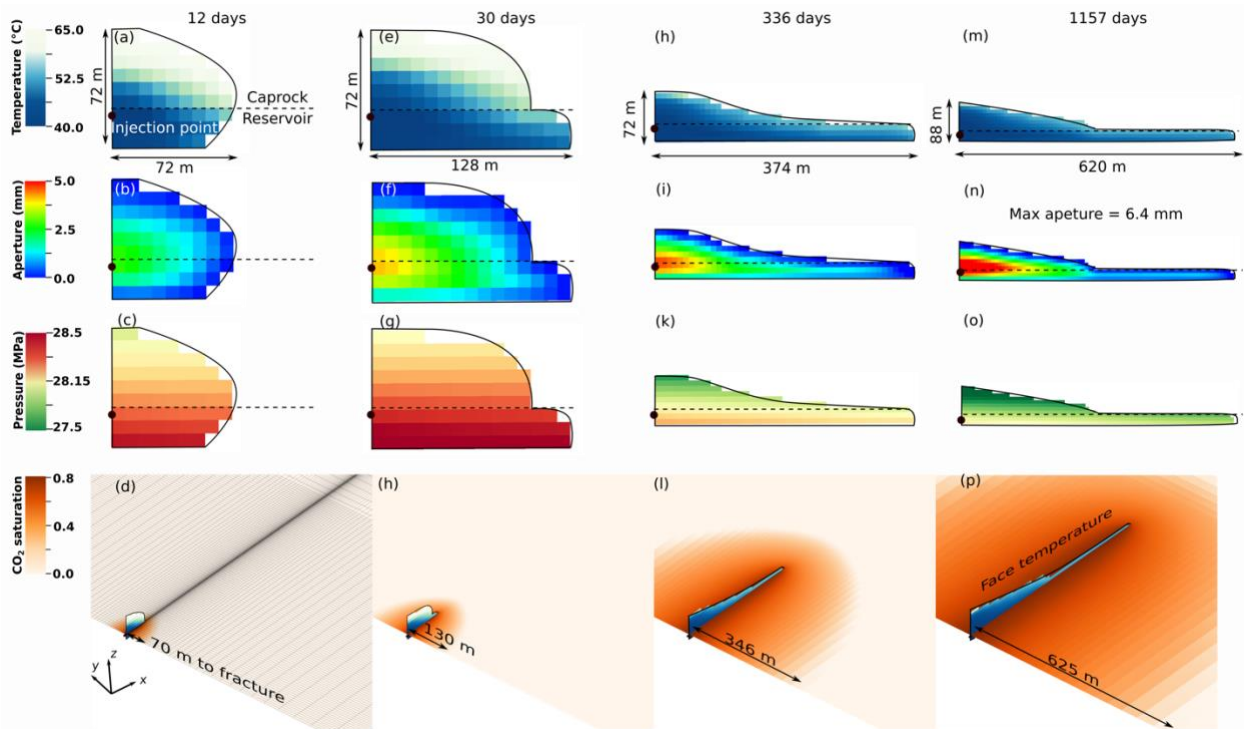
573 at the entrance to the fracture over time, which can be divided into three stages: (1) the initially

574 rapid pressure buildup before apparent fracture growth (about 1 day), (2) the pressure plateau as

575 fracture propagates (from 1 day to 30 days), and (3) the subsequent slow pressure decline (after

576 30 days). In the first stage, accommodating the injection rate requires sustaining an open fracture

577 in the reservoir, which in turn requires a continuously increasing injection pressure, much higher
 578 than original S_{Rsv} , owing to the effect of back-stresses caused by pressure diffusion into the
 579 reservoir (Detourney and Cheng, 1997; Kovalyshen, 2010). Fu et al. (2020) had modeled how
 580 this effect causes rapid increase of injection pressure and eventually causes fracturing of the
 581 caprock.



582
 583 Fig. 8. Four selected states of the hydraulic fracture and the reservoir rock. The first three rows present snapshots of
 584 temperature (first row), aperture (second row), and pressure (third row) on the evolving hydraulic fracture. The last
 585 row shows the spatial-and-temporal evolution of CO₂ (critical state gas phase) in the reservoir ($z=-1510$ m). The
 586 interface between the reservoir and the caprock is denoted by a dark dashed line and the injection point is annotated
 587 as a black dot. Note that scales vary among the columns of the first three rows for clearer visualization, whereas the
 588 four sub-figures in the fourth row use the same scale.

589
 590 Here we mainly focus on the evolution of fracture propagation after caprock fracturing takes
 591 place, which spans the second and third stages as designated in this section. Fig. 8 shows four

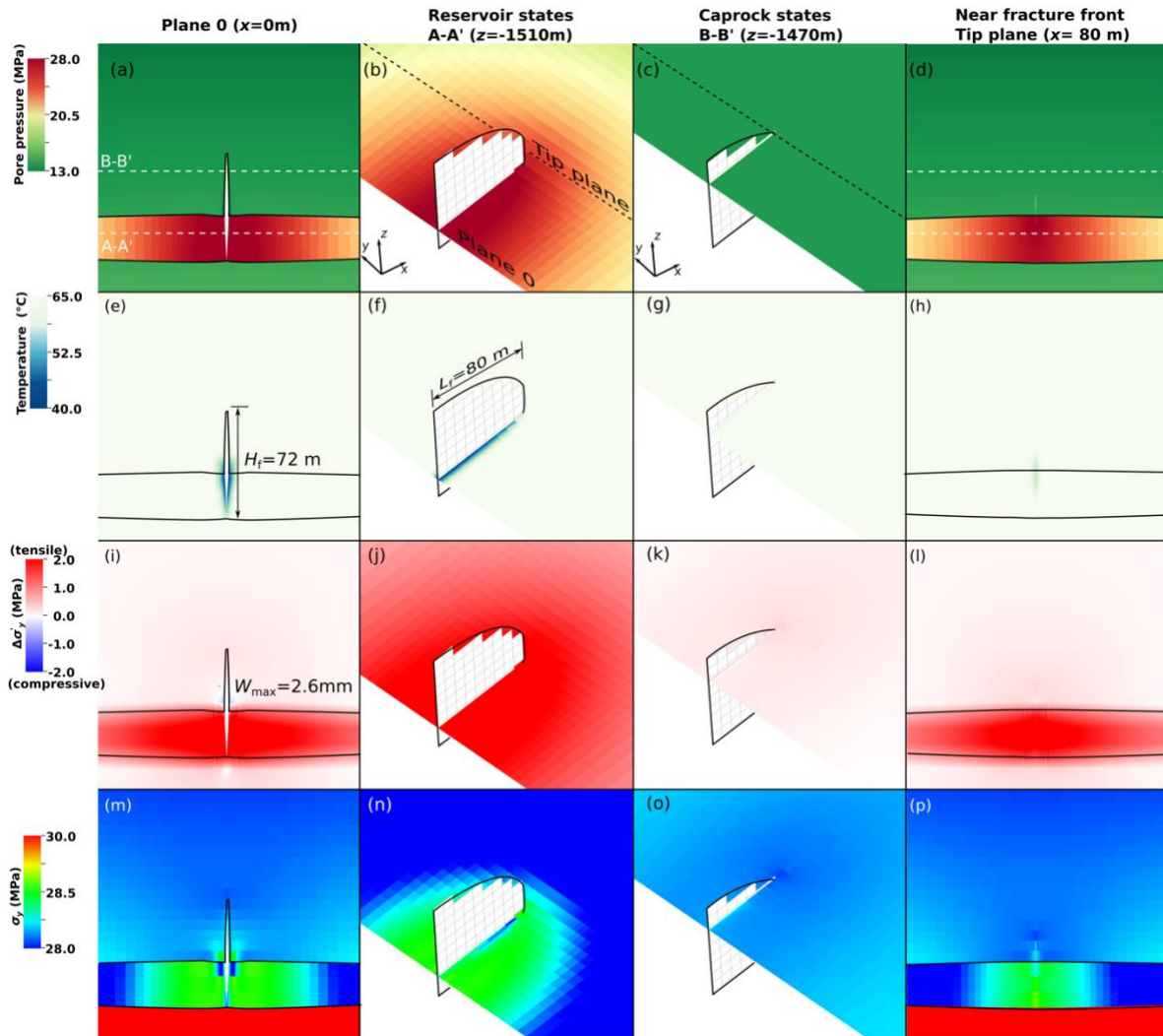
592 representative states of the fluid-driven fracture and CO₂ saturation (supercritical state gas phase)
593 in the reservoir rock, at 12 days (in second stage), 30 days (transition from second to third stage),
594 336 days and 1157 days (both in third stage). In the second stage when the pressure is largely
595 constant, fracturing in caprock seems to lead fracturing in the storage reservoir. The constant
596 injection pressure in this stage reflects the fracturing pressure of the caprock, which is mainly
597 influenced by S_{Cap} . Note that the injection pressure is only slightly higher than S_{Cap} near the
598 reservoir-caprock interface. In the third stage, reservoir fracturing leads the fracture length
599 growth and the injection pressure slowly declines as explained in Section 4.2.2. This pattern
600 change suggests an evolution of fundamental physical mechanisms that dominate fracture growth
601 as elucidated in the subsequent sections.

602

603 **4.2.1 Second stage: caprock fracturing-leading**

604 Fig. 9 presents spatial distributions of the fluid pressure, temperature, effective stress, and total
605 stress in two vertical cross-sections (near the injection and near the fracture tip, respectively) and
606 two horizontal cross-sections (in the reservoir rock 10 m below the bottom of the caprock, and in
607 the caprock 30 m above the top of the reservoir rock) after 12 days of injection. Pore pressure
608 propagates in the reservoir much farther than in the caprock, due to the much higher permeability
609 of the reservoir (150,000 times higher than that of the caprock). Significant temperature
610 decreases only take place within a short distance from the fracture in the reservoir (Fig. 9 (e) and
611 (f)), while temperature change in caprock is hardly perceptible (Fig. 9 (g)). Although thermo-
612 mechanical effect tends to reduce the total stress in the cooled region in the reservoir, the effect
613 of poroelasticity on increasing the total stress in this case is much stronger. As a result, the total
614 stress near the fracture in the reservoir even becomes higher than in the caprock, although initial

615 S_{hmin} in the reservoir was on average 3 MPa lower than that of the caprock. This reversed stress
 616 contrast tends to hamper fracture propagation in the reservoir, favoring easier propagation in the
 617 caprock.

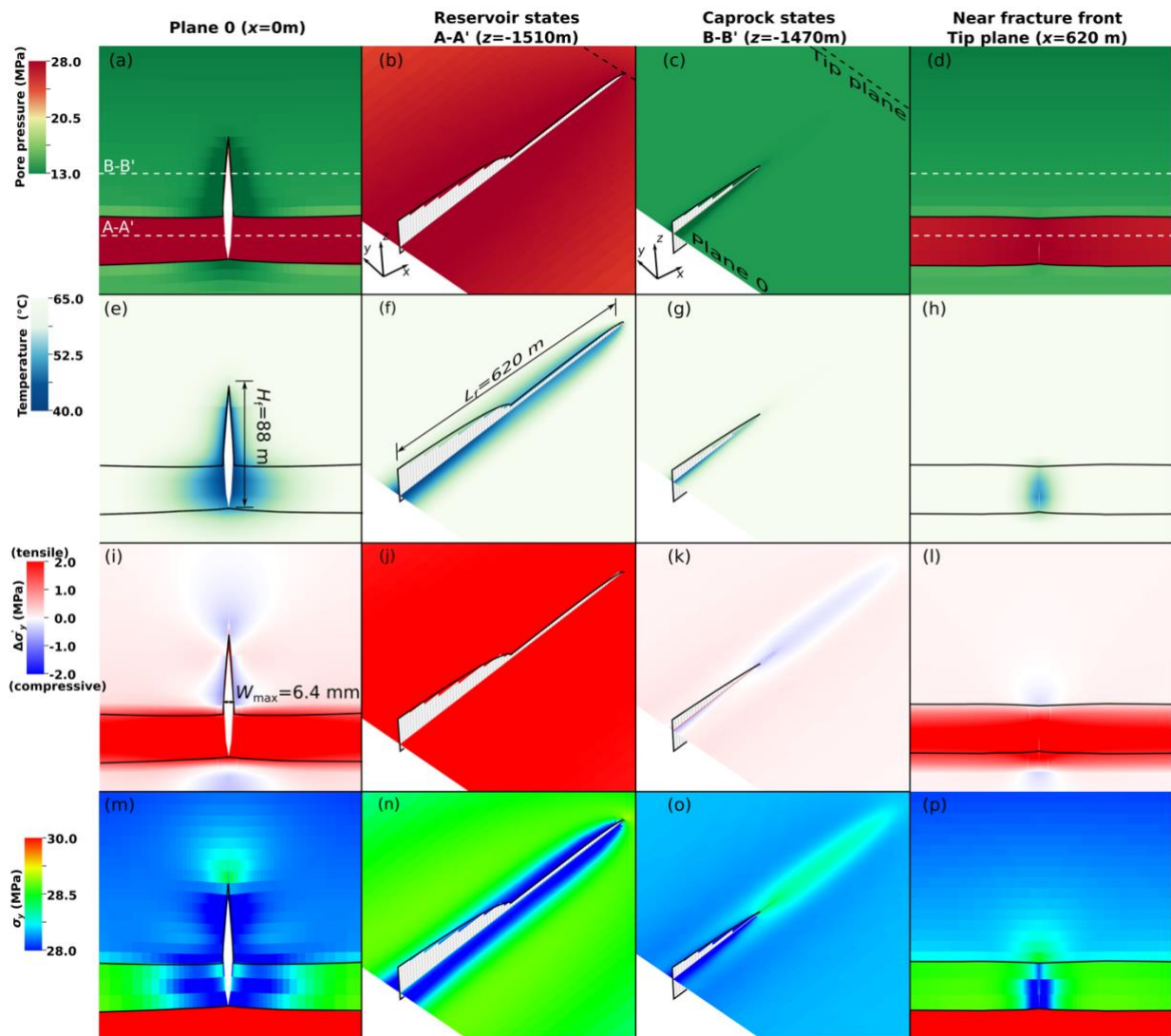


618
 619 Fig. 9. States of the reservoir rock and the caprock after 12 days of injection. The four rows of panels show spatial
 620 distributions of pore pressure (first row), temperature (second row), effective stress increment (third row), and
 621 horizontal total stress (fourth row). The first and fourth columns respectively show the distributions of variables on
 622 two vertical planes cutting the injection point and the fracture tip, respectively. The second and third columns show
 623 the distributions of the variables on two horizontal planes A-A' (reservoir) and B-B' (caprock) respectively. The
 624 deformation of first and fourth columns is magnified by 500 times.

625

626 4.2.2 Third stage: reservoir fracture-leading stage

627 The system response in this stage is depicted using spatial distributions of the same variables as
628 used in the preceding section but for a much later state, 1157 days into the injection (Fig. 10). In
629 general, the most marked difference from the second stage is that the fracture has horizontally
630 grown much longer, which mostly takes place in the reservoir rock, and that the cooling front in
631 the reservoir has advanced much farther (i.e. thermal penetration depth is comparable to fracture
632 height).



633

634 Fig. 10. States of the reservoir rock and the caprock after 1157 days of injection. The four rows of panels show
635 spatial distributions of four variables, namely pore pressure ((a) through (c)), temperature ((d) through (f)), effective
636 stress increment ((g) through (i)), and horizontal total stress ((j) through (l)). The first and fourth columns
637 respectively show the distributions of variables on two vertical planes cutting the injection point and the fracture tip,
638 respectively. The second and third columns show the distributions of the variables on two horizontal planes A-A'
639 (reservoir) and B-B' (caprock) respectively. The deformation of first and fourth columns is magnified by 500 times.
640

641 Unlike the rapid and continuous horizontal propagation, the vertical propagation is slow and
642 contained, since only an absolute height growth of 16 m takes place throughout this stage (Fig.
643 10 (e) and Fig. 7 (b)). This vertical containment of the fracture is mainly because of a favorable
644 stress gradient. The adopted gradient of S_{hmin} such that $-dS_{hmin}/dz < \rho_c g$ provides a relatively
645 stable condition that halts the upward propagation. This is because it takes more hydraulic head
646 for the caprock fracture to grow at a higher position (Fu et al. 2017).

647 Fig. 10(e) shows the cooling front in the reservoir rock has advanced a distance equal to
648 approximately half of the fracture height, nearly 40 m. This results in a significant decrease of
649 total stress perpendicular to the fracture, despite the poromechanical effect that tends to increase
650 the total stress (Fig. 10(n)). Meanwhile, the total stress of regions near the fracture front in the
651 caprock is not reduced by the thermo-mechanical effect but rather slightly increases (fig. 10(o)).
652 This stress increase is mostly owing to the additional compression of the caprock to compensate
653 for the cooling contraction of the reservoir. Other studies have also reported this compression of
654 the caprock induced by the injection of cold CO₂ into the reservoir (e.g. Vilarrasa and Laloui,
655 2015; Salimmda et al. 2017). In this state, the cooling of the reservoir tends to have opposite
656 effects on the total stresses of the reservoir and the caprock. Therefore, the net effect of this
657 discrepancy is that it is much easier to fracture the reservoir rock than the caprock.

658 Another key observation in this stage is a gradually decreasing injection pressure (Fig. 7(a)).
659 This pressure decrease is owing to the effect of cooling on the total stress of the fracture tip
660 region. In the second stage, the fracture tip region, located in the caprock, is largely unaffected
661 by the cooling front (Fig. 9(g)). In this stage, however, the cooling front has traversed the
662 fracture entirely and the near tip region has been cooled, which results in a decrease of total
663 stress (Fig. 10(h) and (p)) and therefore the fracturing pressure decreases.

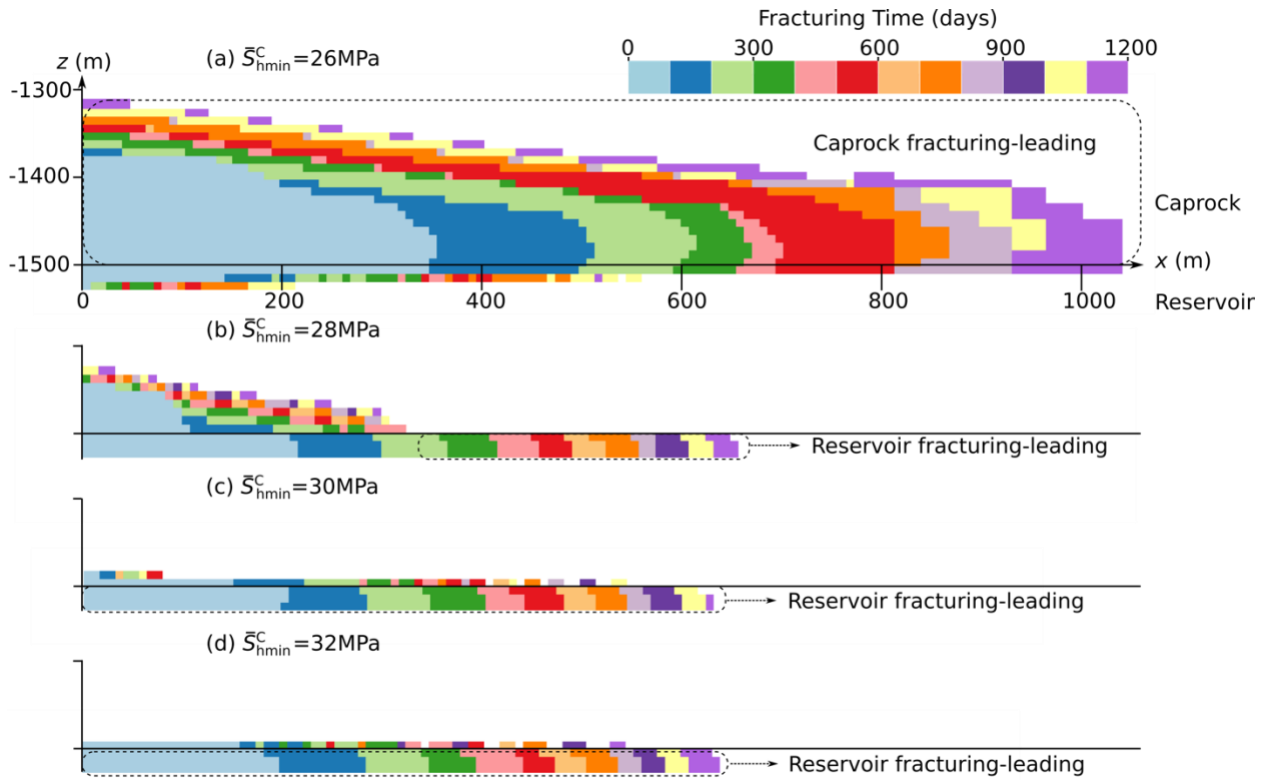
664 Note that in all stages analyzed, the propagation of the fracture is still in the leak-off dominated
665 regime and the mass loss introduced by the coupling scheme is marginal, as clearly shown in
666 Fig.8(a). These results demonstrate that the proposed modeling scheme can be employed to
667 effectively simulate fracture propagation in a leakoff-dominated regime without compromising
668 its accuracy.

669 **5 Effects of the magnitude of *in situ* stresses in the caprock**

670 As reflected in the baseline simulation, the caprock *in situ* stress S_{Cap} plays significant roles in
671 determining the evolution of pumping pressure and affecting the pattern of fracture propagation.
672 However, to what extent the stress difference between S_{Cap} and S_{Rsv} affects the fracture
673 propagation and containment is still unclear. In this section, we evaluate the effects of S_{Cap} on the
674 growth and vertical containment of fluid-driven fractures. Note that $\bar{S}_{\text{hmin}}^{\text{C}}$ presented in this
675 section denotes the greatest horizontal minimum stresses in the caprock, which is the stress level
676 at the interface with the reservoir.

677 Fig. 11 show the effects of $\bar{S}_{\text{hmin}}^{\text{C}}$ (varying from 26 MPa to 32 MPa) on fracture propagation and
678 fracture geometries (i.e. fracture heights and lengths). A lower $\bar{S}_{\text{hmin}}^{\text{C}}$ is expected to reduce
679 vertical containment of caprock fracturing. Especially in the case with $\bar{S}_{\text{hmin}}^{\text{C}} = 26$ MPa, the

680 maximum fracture height reaches around 192 m, far exceeding the thickness of the reservoir (i.e.,
681 24 m). However, the fracture heights (i.e., 32 and 40 m) in cases with $\bar{\sigma}_{hmin}^C = 30$ and 32 MPa are
682 both slightly larger than 24 m and the fracture height (i.e., 88 m) in the baseline lies in between.
683 Meanwhile, the case with $\bar{\sigma}_{hmin}^C = 26$ MPa where caprock fracturing leads the fracture growth
684 throughout the entire simulation has a long fracture length (i.e. 1053 m after 3 year of CO₂
685 injection (Fig. 11(a))), whereas the rest of the cases ($\bar{\sigma}_{hmin}^C = 28$ MPa, 30 MPa, and 32 MPa) have
686 shorter fracture lengths that are similar to each other (i.e. around 650 m at the end of the
687 simulation (Fig. 11(b), (c) and (d))). This discrepancy is caused by the significantly lower leakoff
688 coefficient for the case with $\bar{\sigma}_{hmin}^C = 26$ MPa. First, the difference between the fracture pressure
689 and the pore pressure in the far field is lower in the case with $\bar{\sigma}_{hmin}^C = 26$ MPa compared with the
690 other cases for which pumping pressures are quite similar (Fig. 12(a)). This pressure difference
691 drives fluid leakoff from the fracture to the reservoir. Second, caprock fracturing leads the
692 fracturing process in the low caprock stress case such that the fracture only penetrates into the
693 reservoir a short distance, despite the larger overall height. In addition, the effective leakoff
694 contact area is only a small fraction of the entire height of the reservoir. The combination of
695 these factors determine that the low stress case has a lower leakoff coefficient and therefore a
696 longer fracture length.



697

698 Fig. 11 Effect of the caprock *in situ* stress ((a) 26MPa, (b) 28MPa, (c) 30MPa, and (d) 32MPa) on the distribution of
 699 fracturing time along the fracture. Quantities are projected onto the the x - z plane.

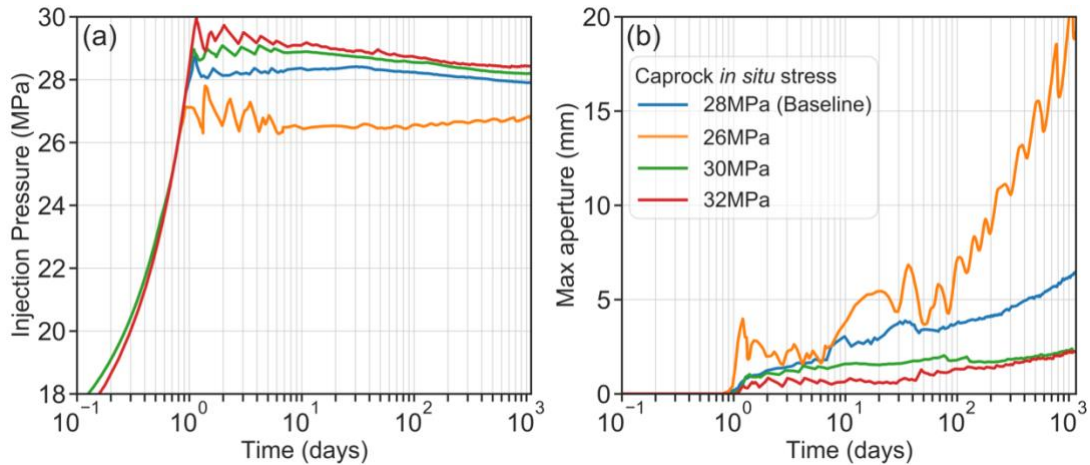
700

701 The magnitude of \bar{S}_{hmin}^C also greatly affects the evolution of injection pressure and maximum
 702 aperture (Fig. 12). When \bar{S}_{hmin}^C is sufficiently high to contain fracturing mostly within the
 703 reservoir ($\bar{S}_{hmin}^C=28, 30, 32$ MPa), the injection pressure, as discussed in the previous section,
 704 experiences first a plateau and then a gradual decline. However, when caprock fracturing leads
 705 the overall fracturing throughout the injection ($\bar{S}_{hmin}^C=26$ MPa), the injection pressure remains
 706 largely constant after the fracture grows into the caprock.

707 Fig. 12(b) shows that maximum apertures in all cases experience continuous increases. Cooling
 708 induced by CO₂ injection in the near wellbore region tends to play convoluted roles in affecting
 709 maximum apertures under different \bar{S}_{hmin}^C levels. For a caprock fracturing-leading case

710 ($\bar{S}_{\text{hmin}}^{\text{C}}=26$ MPa), the fracture-opening pressure, P_f^0 , near the injection point, owing to the
711 thermal-mechanical effect, could drop significantly. However, the fracture propagation pressure,
712 P_p , which is dictated by the caprock *in situ* stress near the fracture front, remains largely
713 unchanged (Fig. 12(a)), thereby causing a high net pressure. This high net pressure, in
714 conjunction with the large overall fracture height, is likely to induce a large fracture aperture in
715 the near-wellbore region. As shown in Fig. 12(b), the maximum aperture in the case with
716 $\bar{S}_{\text{hmin}}^{\text{C}}=26$ MPa reaches around 20 mm. Noticeably, this magnitude of maximum aperture far
717 exceeds the value predicted by isothermal fracture models (McClure and Horne, 2014; Fu et al.,
718 2017). Therefore, employing models that neglect the effects of thermo-elasticity for the
719 simulation of fracturing in GCS will tend to underestimate the magnitude of fracture apertures.

720 For a reservoir fracturing-leading case ($\bar{S}_{\text{hmin}}^{\text{C}}=28, 30, 32$ MPa), however, the fracture opening
721 pressure and the fracture propagation pressure both tend to decrease (Fig. 12(a)). In other words,
722 there might not be a monotonic increase of net pressure at this region as it is in the case with
723 $\bar{S}_{\text{hmin}}^{\text{C}}=26$ MPa, which explains a less remarkable increase of aperture magnitude. Meanwhile,
724 the maximum apertures for cases with $\bar{S}_{\text{hmin}}^{\text{C}}=30$ MPa and 32MPa approach similar values after
725 300 days of injection. This means in the long run, provided the caprock stress is high enough to
726 prevent fracture propagation into the caprock, the exact magnitude does not play a significant
727 role in affecting the system response.



728

729

Fig. 12. Effect of the caprock *in situ* stress on (a) the injection pressure and (b) the maximum aperture. The apparent oscillation in the curves is caused by sudden pressure drop when the fracture propagates by the length of an element: a typical artifact for this type of space discretization scheme.

730

731

732

733 6 Concluding remarks

734

This paper develops an efficient and effective modeling scheme for simulating thermo-hydro-mechanical processes in fluid-driven fracturing. Such a modeling capability is crucial for studying geologic carbon storage (GCS) in reservoirs with marginal permeability where a hydraulic fracture could propagate in both the reservoir and caprock with complex

735

736

737

phenomenology. The model captures multiphase multicomponent fluid flow and heat transfer

738

within fractures and matrix, poro/thermo-mechanical deformation of solid rocks, and fracture

739

propagation. Each of the physical processes is modeled using a robust individual module, and the

740

modules are coupled utilizing a common simulation platform. In order to overcome the

741

numerical challenges posed by coupling many complex processes, we take advantage of some

742

self-stabilizing features of leakoff-dominated fracturing to simplify the numerical coupling.

743

These features enable us to develop a sequential coupling scheme without convergence

744

difficulties. Verification against the PKN solution in the leakoff-dominated regime indicates that

745

746 the simple scheme does not compromise the accuracy of the results for simulating leakoff-
747 dominated fracturing.

748 In simulating a 3D field-scale injection operation loosely based on the In Salah project, the
749 model reveals complex yet intriguing behaviors of the reservoir-caprock-fluid system. Soon after
750 the injection starts, back-stress caused by pressure diffusion in the reservoir drives a sharp
751 increase in injection pressure to keep the fracture open, until the pressure is high enough to drive
752 fracture propagation into the caprock. The injection pressure then remains largely constant at the
753 caprock's fracturing pressure. Injected fluid continued to be fed into the reservoir through the
754 slowly propagating fracture. Meanwhile, temperature decrease in the reservoir gradually reduces
755 the reservoir's total stress, and eventually the fracturing pressure of the reservoir becomes lower
756 than in the caprock. Thereafter the fracture mainly propagates in the reservoir, and the injection
757 pressure slowly declines accordingly. We also used the model to study the effects of the *in situ*
758 stress contrast between the reservoir and caprock on the vertical containment of the fracture.

759 We found many processes, including thermal, hydraulic, and mechanical processes, are involved
760 in fracturing caused by CO₂ injection. These processes have complex interactions and the
761 relative importance among these processes can evolve as injection progresses. The new model
762 proves effective in simulating these processes and their complex interactions in fidelity that is
763 unattainable for existing simple models. For example, thermal contraction induced by CO₂
764 injection has often been speculated to have a negative impact on fracture containment. Our study
765 shows that cold fluid injection itself could actually benefit the geomechanical containment of
766 fracturing under certain stress conditions within the caprock. Our results indicate that a gradual
767 pumping pressure decline can be used as a practical indicator of fracture growth during injection.

768 Despite the success in revealing the complex interactions among multiple physical processes, all
769 the simulations presented in this paper used simplified stress profiles. More realistic stress
770 profiles with layered fabric (Fisher and Warpinski, 2012) and “rough” in situ stress profiles (Fu
771 et al., 2019), should be considered to further assess the caprock integrity and system responses in
772 the future.

773 **Acknowledge**

774

775 This manuscript has been authored by Lawrence Livermore National Security, LLC under
776 Contract No. DE-AC52-07NA2 7344 with the US. Department of Energy. The United States
777 Government retains, and the publisher, by accepting the article for publication, acknowledges
778 that the United States Government retains a non-exclusive, paid-up, irrevocable, world-wide
779 license to publish or reproduce the published form of this manuscript, or allow others to do so,
780 for United States Government purposes. This work is LLNL report LLNL-JRNL-816783.

781

782 **Reference**

783 Bohloli, B., Ringrose, P., Grande, L., Nazarian, B., 2017. Determination of the fracture pressure
784 from CO₂ injection time-series datasets. *Int. J. Greenh. Gas Control* 61, 85–93.

785 <https://doi.org/10.1016/j.ijggc.2017.03.025>

786 Brooks, R.H., Corey, A.T., 1964. Hydraulic Properties of Porous Media. *Hydrology Papers* 3.
787 Colorado State University, Fort Collins, CO.

788 Bungler, A.P., Detournay, E., Garagash, D.I., 2005. Toughness-dominated hydraulic fracture with
789 leak-off. *Int. J. Fract.* 134, 175–190. <https://doi.org/10.1007/s10704-005-0154-0>

790 Eshiet, K.I.I., Sheng, Y., 2014. Carbon dioxide injection and associated hydraulic fracturing of
791 reservoir formations. *Environ. Earth Sci.* 72, 1011–1024. [https://doi.org/10.1007/s12665-013-](https://doi.org/10.1007/s12665-013-3018-3)
792 [3018-3](https://doi.org/10.1007/s12665-013-3018-3)

793 Carrier, B., Granet, S., 2012. Numerical modeling of hydraulic fracture problem in permeable
794 medium using cohesive zone model. *Eng. Fract. Mech.* 79, 312–328.
795 <https://doi.org/10.1016/j.engfracmech.2011.11.012>

796 Coussy, O., 2004. *Poromechanics*. John Wiley and Sons, Chichester, England.

797 Culp, D., Tupek, M.R., Newell, P., Hubler, M.H., 2017. Phase-field modeling of fracture in CO₂
798 sequestration. In: 51st US Rock Mechanics/Geomechanics Symposium. American Rock
799 Mechanics Association ARMA–2017–0644.

800 Fan, C., Elsworth, D., Li, S., Zhou, L., Yang, Z., Song, Y., 2019. Thermo-hydro-mechanical-
801 chemical couplings controlling CH₄ production and CO₂ sequestration in enhanced coalbed
802 methane recovery. *Energy* 173, 1054–1077. <https://doi.org/10.1016/j.energy.2019.02.126>

803 Fu, P., Johnson, S.M., Carrigan, C.R., 2013. An explicitly coupled hydro-geomechanical model
804 for simulating hydraulic fracturing in arbitrary discrete fracture networks. *Int. J. Numer. Anal.*
805 *Methods Geomech.* 37, 2278–2300. <https://doi.org/10.1002/nag.2135>

806 Fu, P., Settghost, R.R., Hao, Y., Morris, J.P., Ryerson, F.J., 2017. The Influence of Hydraulic
807 Fracturing on Carbon Storage Performance. *J. Geophys. Res. Solid Earth* 122, 9931–9949.
808 <https://doi.org/10.1002/2017JB014942>

809 Fu, P., Huang, J., Settghost, R.R., Morris, J.P., Ryerson, F.J., 2019. Apparent toughness
810 anisotropy induced by “roughness” of in-situ stress: A mechanism that hinders vertical growth of
811 hydraulic fractures and its simplified modeling. *SPE J.* 24, 2148–2162.
812 <https://doi.org/10.2118/194359-PA>

813 Fu, P., Ju, X., Huang, J., Settghost, R. R., Morris, J. P., 2019. THM Modeling of Poroelastic
814 Sustainability of Hydraulic Fracture in CO₂ Storage Reservoirs. In *American Rock Mechanics*
815 *Association. In Proceedings of the 44th US Rock Mechanics Symposium*, New York, NY,
816 ARMA-2019-1601, 2019.

817 Fu, P., Ju, X., Huang, J., Settghost, R.R., Liu, F., Morris, J.P., 2020. Thermo-poroelastic responses
818 of a pressure-driven fracture in a carbon storage reservoir and the implications for injectivity and
819 caprock integrity. *Int. J. Numer. Anal. Methods. Geomech.* 1–19.
820 <https://doi.org/10.1002/nag.3165>

821 Francfort, G.A., Bourdin, B., Marigo, J.J., 2008. The variational approach to fracture, *Journal of*
822 *Elasticity.* <https://doi.org/10.1007/s10659-007-9107-3>

823 Francfort, G.A., Marigo, J.-J., 1998. Revisiting brittle fracture as an energy minimization
824 problem. *J. Mech. Phys. Solids* 46, 1319–1342. [https://doi.org/10.1016/S0022-5096\(98\)00034-9](https://doi.org/10.1016/S0022-5096(98)00034-9)

825 Fisher, K., Warpinski, N., 2012. Hydraulic-fracture-height growth: Real data. *SPE Prod. Oper.*
826 27, 8–19. <https://doi.org/10.2118/145949-pa>

827 Garagash, D.I., Detournay, E., Adachi, J.I., 2011. Multiscale tip asymptotics in hydraulic fracture
828 with leak-off. *J. Fluid Mech.* 669, 260–297. <https://doi.org/10.1017/S002211201000501X>

829 Gheibi, S., Vilarrasa, V., Holt, R.M., 2018. Numerical analysis of mixed-mode rupture
830 propagation of faults in reservoir-caprock system in CO₂ storage. *Int. J. Greenh. Gas Control* 71,
831 46–61. <https://doi.org/10.1016/j.ijggc.2018.01.004>

832 Girault, V., Kumar, K., Wheeler, M.F., Wheeler, M.F., 2016. Convergence of iterative coupling
833 of geomechanics with flow in a fractured poroelastic medium. *Comput. Geosci.* 997–1011.
834 <https://doi.org/10.1007/s10596-016-9573-4>

835 Guo, B., Tao, Y., Bandilla, K., Celia, M., 2017. Vertically Integrated Dual-porosity and Dual-
836 permeability Models for CO₂ Sequestration in Fractured Geological Formation. *Energy Procedia*
837 114, 3343–3352. <https://doi.org/10.1016/j.egypro.2017.03.1466>

838 Gor, G.Y., Elliot, T.R., Prevost, J.H., 2013. Effects of thermal stresses on caprock integrity
839 during CO₂ storage. *Int. J. Greenh. Gas Control* 12, 300–309.

840 Haszeldine, R.S., 2009. Carbon Capture and Storage: How Green Can Black Be? *Science.* 325,
841 1647–1652. <https://doi.org/10.1126/science.1172246>

842 Huang, J., Fu, P., Settghost, R.R., Morris, J.P., Ryerson, F.J., 2019. Evaluating a Simple
843 Fracturing Criterion for a Hydraulic Fracture Crossing Stress and Stiffness Contrasts. *Rock*
844 *Mech. Rock Eng.* 52, 1657–1670. <https://doi.org/10.1007/s00603-018-1679-7>

845 Iding, M., Ringrose, P., 2010. Evaluating the impact of fractures on the performance of the In
846 Salah CO₂ storage site. *Int. J. Greenh. Gas Control* 4, 242–248.
847 <https://doi.org/10.1016/j.ijggc.2009.10.016>

848 International Energy Agency. *Energy Technology Perspectives 2010: Scenarios and Strategies to*
849 *2050; 2010*; International Energy Agency, Paris, France.

850 Ju, X., Liu, F., Fu, P., D. White, M., R. Settgest, R., P. Morris, J., 2020. Gas Production from
851 Hot Water Circulation through Hydraulic Fractures in Methane Hydrate-Bearing Sediments:
852 THC-Coupled Simulation of Production Mechanisms. *Energy & Fuels* 0.
853 <https://doi.org/10.1021/acs.energyfuels.0c00241>

854 Kim, J., Tchelepi, H.A., Juanes, R., 2011. Stability and convergence of sequential methods for
855 coupled flow and geomechanics: Fixed-stress and fixed-strain splits. *Comput. Methods Appl.*
856 *Mech. Eng.* 200, 1591–1606. <https://doi.org/10.1016/j.cma.2010.12.022>

857 Kim, J., Moridis, G., Yang, D., Rutqvist, J., 2012. Numerical Studies on Two-Way Coupled
858 Fluid Flow and Geomechanics in Hydrate Deposits. *SPE J.* 17, 485–501.
859 <https://doi.org/10.2118/141304-PA>

860 Kim, J., Moridis, G.J., 2013. Development of the T+M coupled flow-geomechanical simulator to
861 describe fracture propagation and coupled flow-thermal-geomechanical processes in tight/shale
862 gas systems. *Comput. Geosci.* 60, 184–198. <https://doi.org/10.1016/j.cageo.2013.04.023>

863 Howard, G.C., Fast, C., 1957. Optimum fluid characteristics for fracture extension. *Drill. Prod.*
864 *Prac.* 24, 261–270.

865 Li, Z. and Elsworth, D., 2019. Controls of CO₂-N₂ gas flood ratios on enhanced shale gas
866 recovery and ultimate CO₂ sequestration. *J. Pet. Sci. Eng.* 179, 1037-1045.

867 Lecampion, B., Bungler, A., Zhang, X., 2018. Numerical methods for hydraulic fracture
868 propagation: A review of recent trends. *J. Nat. Gas Sci. Eng.* 49, 66-83.
869 <https://doi.org/10.1016/j.jngse.2017.10.012>

870 McClure, M.W., Horne, R.N., 2014. An investigation of stimulation mechanisms in Enhanced
871 Geothermal Systems. *Int. J. Rock Mech. Min. Sci.* 72, 242-260.
872 <https://doi.org/10.1016/j.ijrmms.2014.07.011>

873 Mito, S., Xue, Z., Ohsumi, T., 2008. Case study of geochemical reactions at the Nagaoka CO₂
874 injection site, Japan. *Int. J. Greenhouse Gas Control* 2, 309-318.

875 Moridis, G.J., Freeman, C.M., 2014. The RealGas and RealGasH₂O options of the TOUGH+
876 code for the simulation of coupled fluid and heat flow in tight/shale gas systems. *Comput.*
877 *Geosci.* 65, 56-71. <https://doi.org/10.1016/j.cageo.2013.09.010>

878 Morris, J.P., Hao, Y., Foxall, W., McNab, W., 2011. A study of injection-induced mechanical
879 deformation at the In Salah CO₂ storage project. *Int. J. Greenh. Gas Control* 5, 270-280.
880 <https://doi.org/10.1016/j.ijggc.2010.10.004>

881 Mollaali, M., Ziaei-Rad, V., Shen, Y., 2019. Numerical modeling of CO₂ fracturing by the phase
882 field approach. *J. Nat. Gas Sci. Eng.* 70, 102905. <https://doi.org/10.1016/j.jngse.2019.102905>

883 Nordgren, R.P., 1972. Propagation of a Vertical Hydraulic Fracture. *Soc. Pet. Eng. J.* 12, 306-
884 314. <https://doi.org/10.2118/3009-pa>

885 Orr, F.M., 2009. Onshore geologic storage of CO₂. *Science*. 325, 1656–1658.
886 <https://doi.org/10.1126/science.1175677>

887 Oye, V., Aker, E., Daley, T.M., Kühn, D., Bohloli, B., Korneev, V., 2013. Microseismic
888 monitoring and interpretation of injection data from the In Salah CO₂ storage site (Krechba),
889 Algeria. *Energy Procedia* 37, 4191–4198. <https://doi.org/10.1016/j.egypro.2013.06.321>

890 Pacala, S., Socolow, R., 2004. Stabilization Wedges: Solving the Climate Problem for the Next
891 50 Years with Current Technologies. *Science*. 305, 968–972.
892 <https://doi.org/10.1126/science.1100103>

893 Paluszny, A., Graham, C.C., Daniels, K.A., Tsaparli, V., Xenias, D., Salimzadeh, S., Whitmarsh,
894 L., Harrington, J.F., Zimmerman, R.W., 2020. Caprock integrity and public perception studies of
895 carbon storage in depleted hydrocarbon reservoirs. *Int. J. Greenh. Gas Control* 98, 103057.
896 <https://doi.org/10.1016/j.ijggc.2020.103057>

897 Pan, L., Oldenburg, C.M., Pruess, K., Wu, Y.-S., 2011. Transient CO₂ leakage and injection in
898 wellbore-reservoir systems for geologic carbon sequestration. *Greenh. Gases Sci. Technol.* 1,
899 335–350. <https://doi.org/10.1002/ghg.41>

900 Perkins, T.K., Kern, L.R., 1961. Widths of Hydraulic Fractures. *J. Pet. Technol.* 13, 937–949.
901 <https://doi.org/10.2118/89-pa>

902 Raziperchikolaee, S., Alvarado, V., Yin, S., 2013. Effect of hydraulic fracturing on long-term
903 storage of CO₂ in stimulated saline aquifers. *Appl. Energy* 102, 1091–1104.
904 <https://doi.org/10.1016/j.apenergy.2012.06.043>

905 Ren, F., Ma, G., Wang, Y., Fan, L., Zhu, H., 2017. Two-phase flow pipe network method for
906 simulation of CO₂ sequestration in fractured saline aquifers. *Int. J. Rock Mech. Min. Sci.* 98, 39–
907 53. <https://doi.org/10.1016/j.ijrmms.2017.07.010>

908 Rinaldi, A.P., Rutqvist, J., 2013. Modeling of deep fracture zone opening and transient ground
909 surface uplift at KB-502 CO₂ injection well, In Salah, Algeria. *Int. J. Greenh. Gas Control* 12,
910 155–167. <https://doi.org/10.1016/j.ijggc.2012.10.017>

911 Ringrose, P.S., Mathieson, A.S., Wright, I.W., Selama, F., Hansen, O., Bissell, R., Saoula, N.,
912 Midgley, J., 2013. The in salah CO₂ storage project: Lessons learned and knowledge transfer.
913 *Energy Procedia* 37, 6226–6236. <https://doi.org/10.1016/j.egypro.2013.06.551>

914 Rutqvist, J., Vasco, D.W., Myer, L., 2010. Coupled reservoir-geomechanical analysis of CO₂
915 injection and ground deformations at In Salah, Algeria. *Int. J. Greenh. Gas Control* 4, 225–230.
916 <https://doi.org/10.1016/j.ijggc.2009.10.017>

917 Pruess, K., Tsang, Y.W., 1990. On two-phase relative permeability and capillary pressure of
918 rough-walled rock fractures. *Water Resour. Res.* 26, 1915–1926.
919 <https://doi.org/10.1029/WR026i009p01915>

920 Rutqvist, J., Rinaldi, A.P., Cappa, F., Moridis, G.J., 2013. Modeling of fault reactivation and
921 induced seismicity during hydraulic fracturing of shale-gas reservoirs. *J. Pet. Sci. Eng.* 107, 31–
922 44. <https://doi.org/10.1016/j.petrol.2013.04.023>

923 Salimzadeh, S., Paluszny, A., Zimmerman, R.W., 2017. Three-dimensional poroelastic effects
924 during hydraulic fracturing in permeable rocks. *Int. J. Solids Struct.* 108, 153–163.
925 <https://doi.org/10.1016/j.ijsolstr.2016.12.008>

926 Salimzadeh, S., Paluszny, A., Zimmerman, R.W., 2018. Effect of cold CO₂ injection on fracture
927 apertures and growth. *Int. J. Greenh. Gas Control* 74, 130–141.
928 <https://doi.org/10.1016/j.ijggc.2018.04.013>

929 Salimzadeh, S., Hagerup, E.D., Kadeethum, T., Nick, H.M., 2019. The effect of stress
930 distribution on the shape and direction of hydraulic fractures in layered media. *Eng. Fract. Mech.*
931 215, 151–163. <https://doi.org/10.1016/j.engfracmech.2019.04.041>

932 Senseny, P.E., Pfeifle, T.W., 1984. Fracture toughness of sandstones and shales. In: *The 25th US*
933 *Symposium on Rock Mechanics (USRMS)*. 25–27 June, Evanston Illinois.

934 Settghost, R.R., Fu, P., Walsh, S.D.C., White, J.A., Annavarapu, C., Ryerson, F.J., 2016. A fully
935 coupled method for massively parallel simulation of hydraulically driven fractures in 3-
936 dimensions. *Int. J. Numer. Anal. Methods Geomech.* <https://doi.org/10.1002/nag.2557>

937 Sun, Z., Espinoza, D.N., Balhoff, M.T., 2016. Discrete element modeling of indentation tests to
938 investigate mechanisms of CO₂-related chemomechanical rock alteration. *J. Geophys. Res. Solid*
939 *Earth* 121, 7867–7881. <https://doi.org/10.1002/2016JB013554>

940 Sun, Z., Espinoza, D.N., Balhoff, M.T., Dewers, T.A., 2017. Discrete Element Modeling of
941 Micro-scratch Tests: Investigation of Mechanisms of CO₂ Alteration in Reservoir Rocks. *Rock*
942 *Mech. Rock Eng.* 50, 3337–3348. <https://doi.org/10.1007/s00603-017-1306-z>

943 Vilarrasa, V., Olivella, S., Carrera, J., Rutqvist, J., 2014. Long term impacts of cold CO₂
944 injection on the caprock integrity. *Int. J. Greenh. Gas Control* 24, 1–13.
945 <https://doi.org/10.1016/j.ijggc.2014.02.016>

946 Vilarrasa, V., Laloui, L., 2015. Potential fracture propagation into the caprock induced by cold
947 CO₂ injection in normal faulting stress regimes. *Geomech. Energy Environ.* 2, 22–31.

948 Vilarrasa, V., Rinaldi, A.P., Rutqvist, J., 2017. Long-term thermal effects on injectivity evolution
949 during CO₂ storage. *Int. J. Greenh. Gas Control* 64, 314–322. DOI: 10.1016/j.ijggc.2017.07.019

950 White, J.A., Chiaramonte, L., Ezzedine, S., Foxall, W., Hao, Y., Ramirez, A., McNab, W., 2014.
951 Geomechanical behavior of the reservoir and caprock system at the In Salah CO₂ storage project.
952 *Proc. Natl. Acad. Sci.* 111, 8747–8752. <https://doi.org/10.1073/pnas.1316465111>

953 White, J.A., Castelletto, N., Tchelepi, H.A., 2016. Block-partitioned solvers for coupled
954 poromechanics: A unified framework. *Comput. Methods Appl. Mech. Eng.* 303, 55–74.
955 <https://doi.org/10.1016/j.cma.2016.01.008>

956 Witherspoon, P.A., Wang, J.S.Y., Iwai, K., Gale, J.E., 1980. Validity of Cubic Law for fluid
957 flow in a deformable rock fracture. *Water Resour. Res.* 16, 1016–1024.
958 <https://doi.org/10.1029/WR016i006p01016>

959 Yan, H., Zhang, J., Zhou, N., Li, M., Suo, Y., 2020. Numerical simulation of dynamic
960 interactions between two cracks originating from adjacent boreholes in the opposite directions
961 during supercritical CO₂ fracturing coal mass. *Eng. Fract. Mech.* 223, 106745.
962 <https://doi.org/10.1016/j.engfracmech.2019.106745>

963 Van Genuchten, M.T., 1980. A closed-form equation for predicting the hydraulic conductivity of
964 unsaturated soils. *Soil Sci. Soc. Am. J.* 44 (5), 892–898.